UAB

Universitat Autònoma de Barcelona

UAB

Universitat Autònoma
de Barcelona

Cost-effective electrochemical heavy metal sensors in environmental monitoring and healthcare: from *in-situ* monitoring to a wearable format

Qiuyue Yang

Ph.D. Thesis

Ph.D. in Material Science

Director:
Prof. Arben Merkoçi

Department of Chemistry

Science Faculty

2022

Chapter 3

Chapter 3. GSH to Alleviate Mutual Interference for HMIs Detection
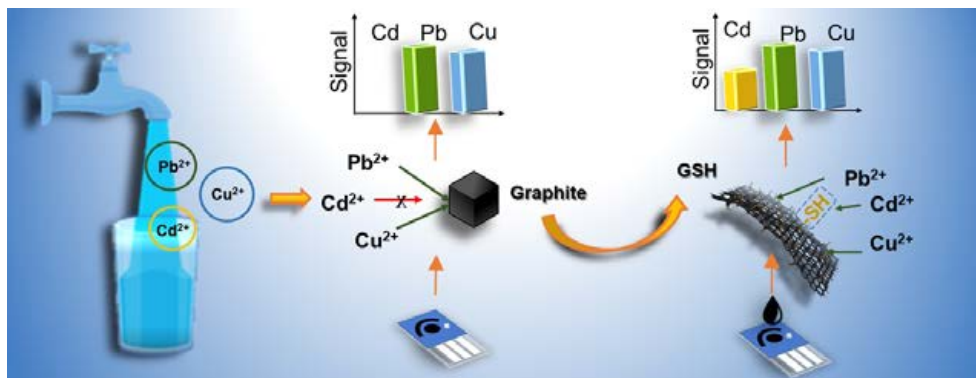
Figure 3.1 Table of Content: For the Cd sensitivity was drastically decreased by the mutual interference of Pb^{2+} and Cu^{2+} in Chapter 2, a new graphene derivative—GSH in which thiol moieties are covalently functionalized on the graphene surface, was employed to modify the WE surface of the SPCE. The GSH-modified SPCE (GSH-SPCE) possessed an enhanced Cd^{2+} sensitivity compared to the bare SPCE, whereas the sensitivity of Pb^{2+} and Cu^{2+} was not influenced.

As discussed in Chapter 1.3, ASV, one of the foremost HMIs sensing techniques, is hindered by the mutual interference issue. In Chapter 2, this issue was intuitively observed that the sensitivity to Cd^{2+} (one of the most toxic heavy metals) was diminished by the other HMIs *i.e.*, Pb^{2+} and Cu^{2+}. Additional metallic particles are frequently required to be embedded in the WE surface of the SPCE to alleviate the effect. However, this approach faces unsustainability with recycling issues. In this study, a metal-free cysteamine covalently functionalized graphene (GSH), was employed to selectively enhance a 6-fold boost in the Cd^{2+} sensitivity of SPCE, while the sensitivity to Pb^{2+} and Cu^{2+} was not influenced in simultaneous detection. The selective enhancement was attributed to grafted thiols on GSH, which have a good affinity to Cd^{2+} based on *Pearson's hard and soft acid and base* principle. Moreover, GSH-SPCE featured high reusable times (23 times) due to the covalent functionalization of thiols, surpassing the state-of-art SPCEs modified by non-covalently functionalized graphene derivatives. Finally, GSH-SPCE was validated in tap water.

The main body of this study is organized with the strand of comparing the sensing performance between GSH-SPCEs and bare SPCEs in simultaneous multi-HMIs detection, with other less-correlated results demonstrated in the followed supporting information briefly.

3.1   Introduction

Heavy metal (HM) pollutants, one of the most released contaminants, influence the critical access to clean water for human health due to their tendency of bioaccumulation, biomagnification as well as environmental persistence.[1,2] On the Environmental Quality Standards Directive List, As, Cd, Cr, Cu, Fe, Ni, Pb, Hg, and Zn are underlined as key substances for evaluating water quality.[3] As mentioned in Chapter 1.3, although some HM elements are necessary for human health (*e.g.* Cu), the ingestion of these HMs at a high concentration can be harmful,[4,5] while other HMs, such as Cd and Pb, are toxic and harmful to the ecosystem even at the ppb range, and bioaccumulate in the human body *via* the foods we eat.[5] Thus, the analysis of HMIs within primary food sources (*e.g.* tap water) is important. Owing to simplicity and low cost, electrochemical techniques are ideal for HMIs analysis. Amongst them, square-wave anodic stripping voltammetry (SWASV) is appealing, for its sensing performance is less influenced by dissolved oxygen in real samples.[6,7]

In the SWASV technique, carbon-based electrodes have gradually replaced hanging mercury drop electrodes (HMDE) due to the toxicity of Hg.[8] However, in comparison to HMDEs, bare carbon electrodes suffer from mutual interference due to the lack of an effective working surface (*e.g.* metal films or functional groups), which induces ion competition and the formation of intermetallic compounds.[8–10] As shown in Chapter 1.3, mutual interference often results in unexpected outcomes, including the drastic decrease of sensing signal, peak shifting, peak splitting, and peaks overlapping.[11] In particular, the sensitivity to Cd^{2+} is decreased by the presence of Pb^{2+} or Pb^{2+} and Cu^{2+} using SPCE,[12,13] GCE,[14] and BDD.[15] Mutual interference renders the detection of Cd^{2+} ions, co-existing with these HMIs, incredibly challenging. If using

SPCEs, addressing this issue is more daunting, due to the rough and non-uniform surface of the SPCE limited by its fabrication, compared to the other carbon electrodes such as the GCE and BDD. A typical strategy is to pre-deposit metal thin films or to embed nanoparticles (*e.g.*, Hg and Bi) onto the WE to mimic the HMDE. [11,16] However, the involved metals render the technique unsustainable with recycling and toxicity issues. Besides, cycling reusability is a second issue. When HMIs deposit on the surface of the metallic electrode surface, the alloy of these two metals could form; during stripping, the alloy is then released into the solution, which causes the loss of the sensing material. Few reusable times (~10 times) of these electrodes have been found, which is limited considering their potential application of *in-situ* measurement in a sensing network. [17–19]

Fortunately, instead of metallic additives, bio- and carbon-based materials rich in N, S and O seem to address the issue due to good affinities toward specific HMIs with the independence of metals. For example, Pérez-Ràfols et al. reported glutathione functionalized SPCE by electrografting, which showed better Cd^{2+} sensitivity with the presence of Pb^{2+} ions in simultaneous detection. However, electrografting required complicated procedures to modify the surface of SPCEs, which limited mass production. [20] Choi et al. applied graphene oxide (GO) doped by diaminoterthiophene (as a carrier of amines) to modify SPCE. The functionalized graphene enhanced the sensitivity of Cd^{2+} in simultaneous detection of Cd^{2+}, Hg^{2+}, Cu^{2+} and Pb^{2+}. [21] However, poor reusability and stability were found, which may perhaps stem from the non-covalent functionalization. Thus, robust bio-functionalized nanomaterials offering high reusability and ease of fabrication are highly sought.

As shown in Chapter 1.2.3, graphene as a 2DNM seems a good candidate for bio-functionalization due to its large basal surface. [22] The functionalization of graphene is primarily divided into non-covalent and covalent functionalization. [23] Non-covalent functionalization takes advantage of the π-interaction between graphene and functionalization reagents, while covalent functionalization creates more robust chemical bonds between the two. Covalent moieties are extremely stable on the graphene surface, which would facilitate better reusability for SPCEs. [24] Accordingly, covalently bio-functionalized graphene derivatives seem promising to address both mutual interference and reusability issues. Nevertheless, the commonly used precursors, graphene oxide (GO) and reduced graphene oxide (rGO), pose the challenge of homogeneous and manageable functionalization due to the non-uniform distribution of oxidized groups. [25,26]

As such, a new methodology of covalently functionalized graphene has been investigated with fluorographene (FG) as the precursor, in which the distribution of fluorine is highly uniform. [27] The nucleophilic substitution reaction on FG is accompanied by defluorination, enabling a facile pathway for controllable graphene chemistry. [28] For example, a graphene derivative named graphene acid (graphene functionalized with carboxylic groups, GA) was prepared *via* the mild hydrolysis of cyanographene which was synthesized from the FG and afforded a practically fluorine-free graphene derivative with covalently bonded nitrile groups. [29] Carboxyl

groups on the GA then behaved as versatile anchoring sites to conjugate with many biomolecules *via* the peptide bond. These derivatives have been utilized in many interesting applications, like energy storage,[30] sensing,[31] and catalysis.[32] Even more excitingly, organic amines, who commonly appear in bio-materials, are known to be good nucleophiles,[33] and they can react with the FG, affording materials with molecules grafted on the graphene backbone directly *via* the covalent bond of the amino group with the graphene surface. This opens the way to the facile and flexible functionalization of graphene with various biomolecules.

This study is the first report to use the covalent functionalization strategy to synthesize a cysteamine functionalized graphene (GSH), which was then modified on the SPCE, aiming for solving the mutual interference issue. The role of GSH in HMIs' sensing performance was investigated by the FSS described in Chapter 2 for *in-situ* and automatic measurements based on SWASV (Figure 3.2a,b). Compared to the bare SPCEs, the GSH-modified SPCE (GSH-SPCE) achieved a selective enhancement of the Cd^{2+} sensitivity. The benchmarking of GSH against the graphene derivatives functionalized with other groups verified its superior sensitivity to Cd^{2+} by leveraging the binding proclivity of thiol residues on GSH toward the softer Cd^{2+} based on *Pearson's hard and soft acid and base* principle (HSAB, in Figure. 3.2c). Moreover, continuous measurements were tested by GSH-SPCE with expectations of better reusability due to the covalent functionalization. Lastly, GSH-SPCE was used to challenge the real sample of tap water.
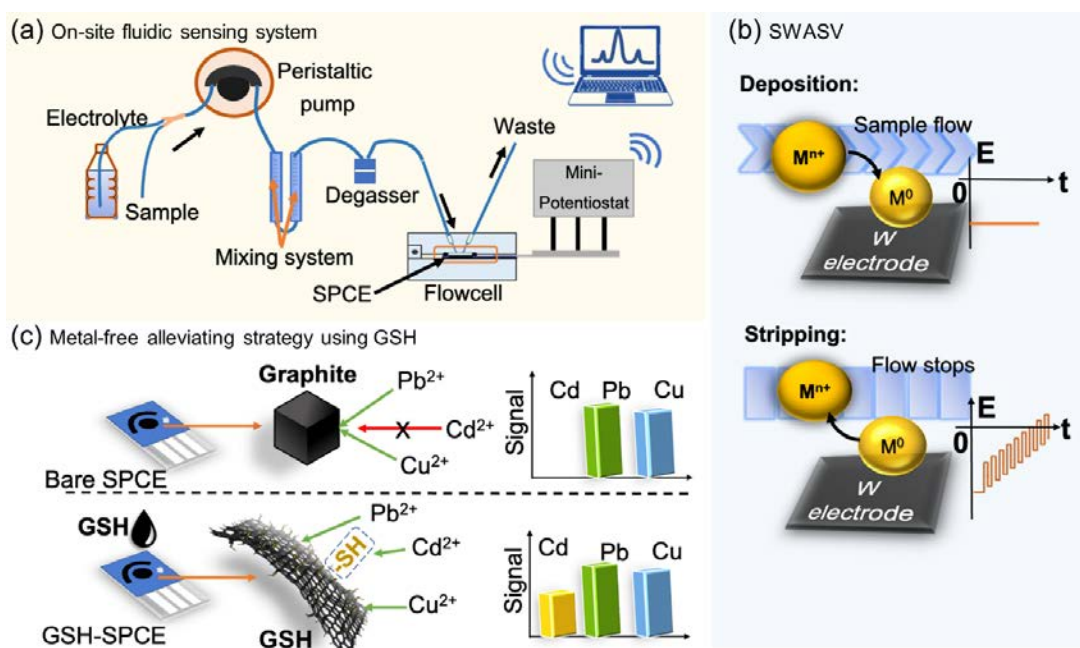

Figure 3.2 Schematic illustration of sensing system: (a) the FSS used for *in-situ* HM detection, allowing the sample and supporting electrolyte to mix automatically and to flow through the surface of SPCE in the deposition step with the stopped flow in the stripping step during SWAVS, (b) the main two steps of SWASV including deposition, and stripping steps, and (c)

GSH for Cd^{2+} sensing enhancement compared with bare SPCE by the functionalized cysteamine moieties and graphene-like 2D structure.

3.2   Experimental Section

3.2.1   Reagents and Equipment

The SPCEs were fabricated as the same protocol in Chapter 2. Briefly, Ag/AgCl ink was Loctite EDAG AV458, Henkel, carbon paste was C2030519P4 CARBON SENSOR PASTE (267508), Sun Chemical, Ag ink was C2180423D2 SILVER PASTE 349288, Sun Chemical, and insulating ink was D2070423P5 DIELECT PASTE GREY, Sun chemical. Deionized water (18.2 MΩ·cm at 25 °C, Milli-Q) was used throughout all the experiments. 37% Hydrochloric acid was 320331-2.5L from Sigma. Standard HM solutions (Cd^{2+}, Cu^{2+}, and Pb^{2+} 1000ppm, Sigma) were all AAS grade. GO aqueous solution (N002-PS-1.0) was acquired from Angstron Materials, Dayton, OH, USA.

The concentration of various graphene derivatives' supernatants was estimated by UV-VIS spectrophotometry (UV-1900, Shimadzu). The morphology of the material was characterized by SEM analysis with Hitachi SU6600 instrument with an accelerating voltage of 5 kV, and TEM analysis with a JEM 2010 TEM instrument (Jeol, Japan). The FTIR characterization was operated on an iS5 FTIR spectrometer (Thermo Nicolet), equipped with a Smart Orbit ATR accessory with ZnSe crystal. The material was characterized by XPS technique (PHI VersaProbe II (physical electronics) spectrometer using an Al Kα source (15 kV, 50 W), the MultiPak (Ulvac-PHI, Inc.). Software package was used to evaluate the obtained data. Raman analysis was operated on a DXR Raman microscope using the 633 nm excitation line of a diode laser. The spiked tap water was analyzed in a 7500ce inductively coupled plasma mass spectrometry (ICP-MS) instrument (Agilent).

3.2.2   Synthesis of GSH

2 g of graphite fluoride (61< at. % F, polymer, Sigma-Aldrich) was dispersed in 120 ml of DMF (for peptide synthesis, Merck) in a round-bottom flask (250 mL) and stirred at room temperature using a magnetic stirring bar for 72 h. Then, the dispersion was sonicated in an ultrasonication bath for 4 h with the temperature kept below 60°C and was left stirring for another 24 h at room temperature. In the last step, 10.2 g K_2CO_3 (Penta) and finally 5 g cysteamine (Sigma-Aldrich) were added to the dispersion with stirring and heating at 130°C in an oil bath for 24 h in the hood, equipped with a condenser for reflux.

When cooling down to room temperature, the product was centrifuged and washed with DMF (2x), hot DMF (1x), acetone (2x), hot acetone (1x), ethanol (3x), distilled water (2x) and hot distilled water (1x) by centrifugation (20000 rcf/10min) and subsequent addition of fresh solvent to the solid product that was then redispersed under sonication.
For the decomposition of possible unwanted disulfide bonding in the final product structure, the whole amount of the synthesized material was mixed with 420 μL of 2-mercaptoethanol (Carl Roth; ~2x molar ratio of -SH groups considered as 20 % F.D.), being shaked for 30 minutes,

and then the material was additionally washed with ethanol (1x), acidified distilled water (2x) and distilled water (1x) using centrifugation (20000 rcf/10min). The purification procedure of the synthesized product was finalized by placing the product into a dialysis membrane (cut-off 14kDa), which was in 5 L of distilled water. The water was changed every day until the dispersion (containing the GSH) reached the conductivity <100 µS/cm (provided by the conductivity standard solution, 100 µS/cm, NaCl, 50 mL).

3.2.3   Preparation of GSH-SPCEs

SPCEs were fabricated using a layer-by-layer strategy: the silver ink, silver/silver chloride paste, carbon paste, and dielectric paste were printed with their corresponding patterns on the PET substrate. More information has been reported in our previous study and Chapter 2.[34]

For better quality control, all SPCEs were cleaned in 0.05 M HCl and deionized water, and then were pre-tested by SWASV. Based on the obtained stripping curves (Charge vs Potential), the SPCEs were selected within the charge range of 2-4 mC. Additional cyclic voltammetry (10 scans) was performed by the selected SPCEs in 0.05 M HCl for further cleaning.

The suspension of graphene derivatives (GSH, GA, and GO, 1 mg ml^{-1}) was sonicated in a bath for 30 min at room temperature. Then, the suspension was centrifuged at 9000 rpm for 1 min. 5 µL of GSH supernatant (~0.016 mg ml^{-1}) was pipetted onto the working electrode and dried in the oven at 37°C. Depending on the final modified volume (10 µL, 15 µL, and 20 µL), the drop-casting procedure was repeated several times in a 5 µL increment. Other graphene derivatives' (GA and GO) supernatants were drop casted on the SPCE with the same method except for adjusting their concentrations to be equal to that of the GSH supernatant. All the concentrations of supernatants were estimated with UV-Vis by the Beer-Lambert law, where the molar absorptivity is 3463 ml (mg m)$^{-1}$.[35] GO-SPCE was reduced (to rGO-SPCE) in cyclic voltammetry (CV, 10 scans) between -1.1 and 0 V, and then by chronopotentiometry at −1.1 V for 200s.

3.2.4   HMIs Detection by SPCEs

HM analysis was conducted in the FSS reported in Chapter 2 and our previous study for *in-situ* and automatic measurement.[34] Figure 2.3 explains the working principle of the sensing system in detail. The parameters of stripping square waves remain the same as shown in Table 2.1: the frequency of square waves is 25 Hz with an amplitude of 30 mV and a potential step of 6 mV (Estep). The equilibrium time was 20s.

3.2.5   Data Analysis

The integral area under each peak (A) was used as the sensing signal instead of the peak current due to the peak splitting issue of the Pb^{2+} oxidative peak. A was calculated by the software PStrace 5.8 (PalmSens). LOD was estimated based on the International Conference on Harmonization's Q2 Validation of Analytical Procedures.[20]

$$LOD=3\sigma/S$$

where σ and S are the intercept standard error and slope of the calibration line, respectively, obtained by Origin 2018. Sensitivity (S) was defined as the calibration slope. Repeatability was defined as the relative standard deviation (RSD) of the sensing signals from continuous measurements. The reproducibility is the RSD of the sensitivities collected from different SPCEs. The t-test used was 2-tailed Student's t-test with heteroscedasticity conducted in Microsoft Excel. Recovery was calculated by the tested concentration divided by the spiked concentration.[36]

3.3   Results and Discussion

3.2.6   Synthesis and Characterizations of GSH

GSH was synthesized through the substitution of fluorine on the FG by the amino groups (-NH_2) on cysteamine (Figure 3.3a), where the defluorination and functionalization occurred simultaneously due to the nucleophilic substitution ability of fluorine to nucleophiles.[37] To secure the deprotonation of the amino groups (thus their maximum nucleophilicity), potassium carbonate (K_2CO_3) was used as a base to scavenge protons from the system, which also prevented the formation of the by-product hydrogen fluoride (HF) during synthesis. Additionally, K_2CO_3 boosted the surface area of the resulting material thanks to the release of carbon dioxide (CO_2) during the reaction. [38]

The SEM and TEM images in Figure 3.3b-d) demonstrate the typical 2D sheet of functionalized graphene with a wrinkled morphology.

FTIR results show that GSH was a fluorine-free graphene-based material, due to the absence of a sharp feature at 1200 cm^{-1} originating from C-F bond vibration, which was clearly apparent in the pristine graphite fluoride (GF, in Figure 3.3 e). The development of sp^2 regions was evident from the strong C=C band at 1570 cm^{-1}. The broad feature in the region between 1300 and 1050 cm^{-1} was common for many graphene-based materials, representing a large group of vibration modes. Most of the features represent graphene in-plane C-C bond stretching,[29] while C-S bonding can be found, according to the previous results, between 1150 and 1180 cm^{-1}.[39,40] The shoulder at 1450 cm^{-1} was assigned to C-H bending which was the only proof of the presence of C-H bonds since the C-H stretching band at 2900 cm^{-1} was barely observable.[38] The shoulder at 1025 cm^{-1} may be assigned to the C-N bond vibration of the aliphatic amines.[41] Although this feature might also represent the oxygen contamination, specifically the C-O alkoxy bond, the band aside at lower wavenumber seems to be assigned more in favor of the C-N bond rather than the C-O bond whose band should be at higher wavenumbers.[42]
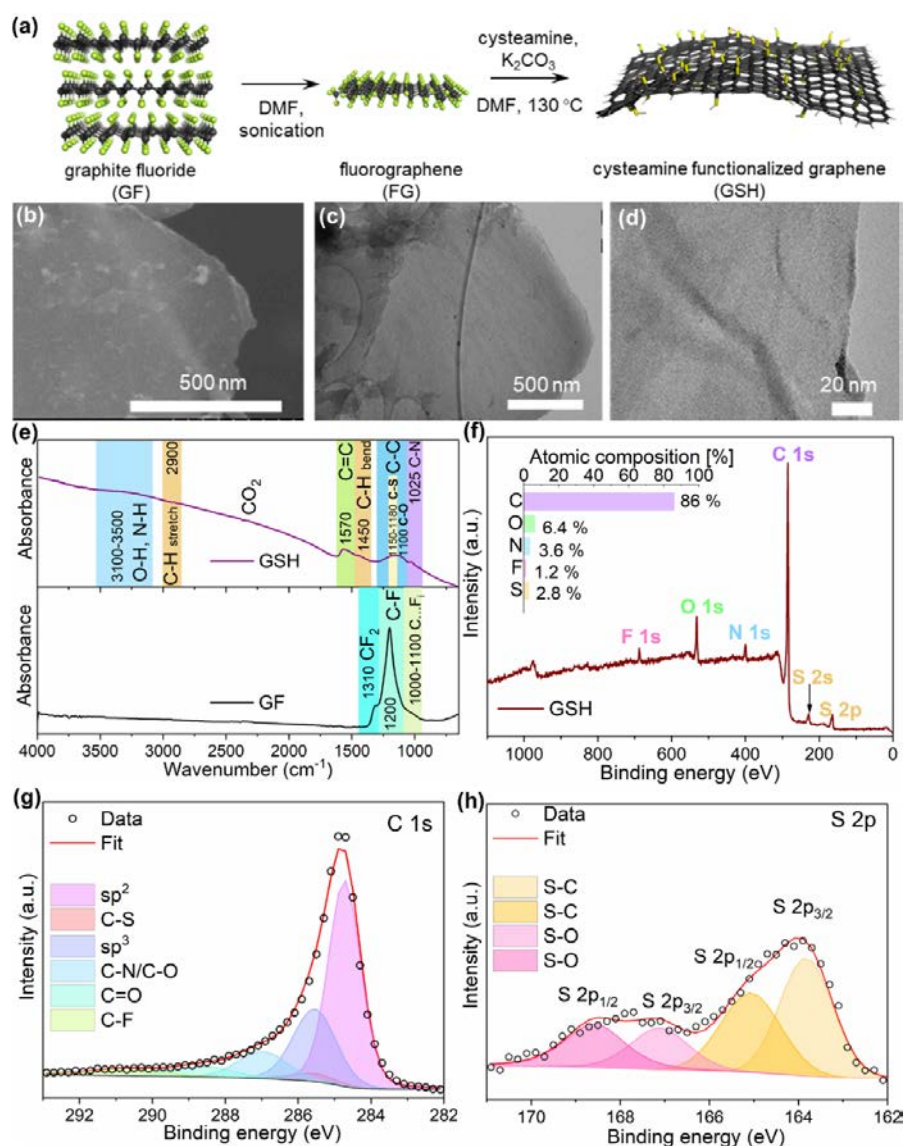
Figure 3.3 Characterizations of GSH. (a) Schematic illustration of GSH synthesis. (b) The scanning electron microscopy (SEM), (c) transmission electron microscopy (TEM), and (d) magnified TEM images of the GSH sheet. (e) Fourier-transform infrared spectroscopy (FTIR) spectra of GSH and graphite fluoride (GF). (f) X-ray photoelectron spectroscopy (XPS) survey spectrum and element composition analysis. High resolution XPS spectra for (g) C 1s, and (h) S 2p.

The elemental composition of GSH in XPS (Figure 3.3f) further verifies that the GSH was nearly fluorine-free (1.2 at. %), containing C, N, and S atoms, which complies with the results of FTIR. The minimal oxygen content could originate from either DMF molecules reacting with the GF during functionalization,[29] or adventitious contamination from the environment. The functionalization degree (F.D.) was estimated to be 3.5% based on the S/C ratio as reported elsewhere.[29] In the C 1s region of the XPS spectrum (Figure 3.3g), carbon atoms were found mainly in the sp^2 hybridization state, further proving the graphene-like structure of the GSH observed from the FTIR results, while other components found at higher binding energy corresponded to the sp^3-hybridized carbon, mostly from the alkyl chains of the cysteamine

functionalities, and the carbon bonded to sulfur, nitrogen, oxygen and residual fluorine atoms with primarily overlapping binding energy values.

The deconvolution of the S 2p envelope shows that sulfur atoms were mostly bonded to carbon atoms due to the component at 163.9 eV for S $2p_{3/2}$, which further proves the successful functionalization of the material. However, part of the sulfur atoms was found to be bonded to oxygen atoms, evident from the presence of additional components at a higher binding energy value (Figure 3.3h).[43]

The Raman spectrum of GSH (Figure S3.1) exhibited a broad D band and rather high I_D /I_G ratio (1.26), denoting that the material contained a high number of defects within the graphene backbone. It should stem mainly from the sp^3 carbons signifying the formation of the bond between the cysteamine functionality and the graphene sheet, thus reflecting a high F.D. of the prepared material. Moreover, the sharp G-band shows that the material had a developed network of sp^2 carbon signifying a high degree of reductive defluorination, which also accords with the C 1s spectrum in XPS that carbon sp^2 hybridized atoms constituted a dominant fraction (Figure 3.3g).

Overall, the characterization results of the GSH conclude that the reaction of FG with cysteamine afforded graphene-like material functionalized with thiol functionalities. This is thanks to the covalent bond of the cysteamine molecules to the graphene surface *via* the amino groups.

3.2.7   Sensing Performance of GSH-SPCE Compared to Bare SPCE

3.2.7.1   Optimization and Sensing Performance in Individual HM Standard Solutions

The GSH-SPCE was prepared by drop casting, in which the GSH supernatant (~0.016 mg ml^{-1} estimated by UV-Vis) was pipetted on the WE of the SPCE. After the supernatant completely evaporated, the procedure was repeated once to achieve a better modification.

All the following experiments were operated under the optimized situation, *i.e.,* HCl as supporting electrolyte of 0.05 M, the pipetted GSH supernatant volume of 10 µL, and deposition potential of -1.0 V with a flow rate of 3 ml·min^{-1} and flow time of 200s. The optimization results are discussed and shown in Figure S3.2-S3.4 and Table S3.1.

A comparison study between GSH-SPCE and bare SPCE was operated in the individual solution of Cd^{2+}, Pb^{2+} and Cu^{2+} first. When tested in the individual HM solutions (Figure S3.5), the GSH-SPCE clearly showed higher sensing signals at each concentration for all the HMIs compared to the bare SPCE, which complies with the fact that GSH offers faster charge transfer rates with lower charge transfer resistance, as shown in the cyclic voltammetry (CV) and electrochemical impedance spectroscopy (EIS, Figure S3.6, and Table S3.2).

3.2.7.2   Detection of Cd^{2+} Under the Interference of Pb^{2+} and Cu^{2+}

Cd^{2+} is the most difficult HMIs to detect in the simultaneous detection of Cd^{2+}, Pb^{2+} and Cu^{2+} ions due to its diminished sensitivity in the presence of the other two as found in the previous Chapter (Figure 2.9 in Chapter 2). It could be attributed to two factors: 1) as discussed in Chapter 1.4, Cd^{2+} ions requiring a more negative potential during deposition tend to deposit on the metallic surface of Pb and Cu with less depositing potential, rather than on the carbon electrode, which may induce the signal loss and formation of intermetallic compounds (*e.g.*, Cd-Pb, Cd-Cu, and Cd-Pb-Cu),[44] and 2) the ions' competition during deposition as reported elsewhere. [11,45] Hence, first we investigated the influence of Cu^{2+} and Pb^{2+} separately on the Cd^{2+} sensing signals.

The GSH-SPCE and bare SPCE were tested in 80 ppb Cd^{2+} with different concentrations of Cu^{2+} or Pb^{2+} ranging from 0 to 160 ppb. Figure 3.4a demonstrates that Cd^{2+} signals of the GSH-SPCE fluctuated slightly with varying concentrations of Cu^{2+}, which indicates that the Cd-Cu alloy doesn't strongly influence Cd^{2+} signals. Regarding the evaluation of Pb^{2+} interference in Figure 3.4b, the GSH-SPCE was able to detect Cd^{2+} while bare SPCE only showed unmeasurable signals, denoting that the GSH alleviated the Pb^{2+} interference on Cd^{2+} significantly and allowed for simultaneous detection of both, which was incredibly difficult for the bare SPCE.
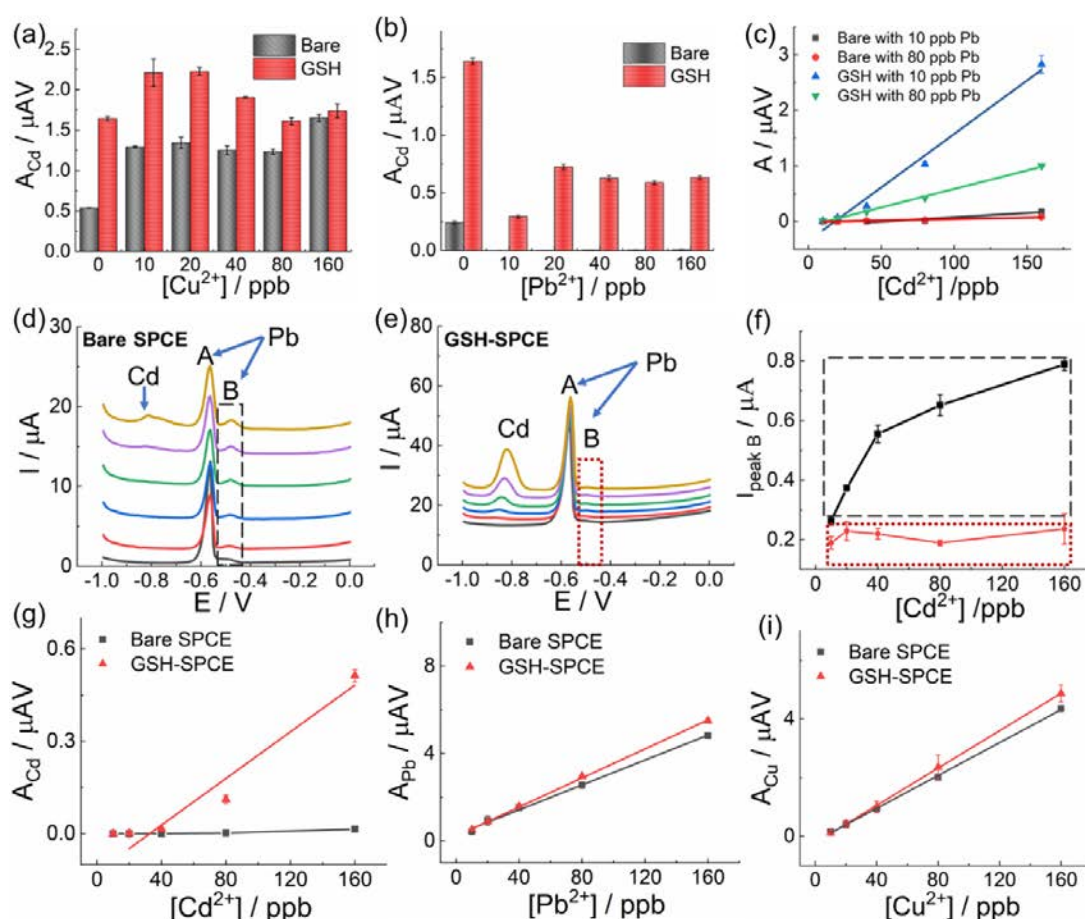

Figure 3.4 The sensing performance of GSH-SPCE and bare SPCE to Cd^{2+} under mutual interference of Pb^{2+} and Cu^{2+}. The peak areas of 80 ppb Cd^{2+} by GSH-SPCE and bare SPCE with (a) various concentrations of Cu^{2+} and (b) Pb^{2+} respectively. (c) The calibration curves of Cd^{2+} in GSH-SPCEs and bare SPCEs with Pb^{2+} as interfering ions of 10 ppb and 80 ppb. The

voltammograms of (d) bare SPCE and (e) GSH-SPCE detect various concentrations of Cd^{2+} (from 0 (black) to 160 ppb (yellow)) simultaneously with 80 ppb Pb^{2+} (f) The peak B maxima of GSH-SPCE (red rectangle) and bare SPCE (black rectangle) with the varying concentration of Cd^{2+}. The calibrations of bare and GSH-SPCEs toward (g) Cd^{2+} under the interference of 80 ppb Pb^{2+} and Cu^{2+}, (h) Pb^{2+} under the interference of 80 ppb Cd^{2+} and Cu^{2+}, and (i) Cu^{2+} under the interference of 80 ppb Cd^{2+} and Pb^{2+}.

Furthermore, to investigate whether the Cd^{2+} sensitivity is influenced by the Pb^{2+} concentration, the GSH-SPCE and bare SPCE were used to detect various concentrations of Cd^{2+} in two scenarios with the presence of 10 ppb and 80 ppb Pb^{2+}. The GSH increased the sensitivity of the bare SPCE to Cd^{2+} in both scenarios in Figure 3.4c; however, it is noteworthy that the GSH was limited to fully resist mutual interference, for the sensitivity of the GSH-SPCE to Cd^{2+} also decreased at the higher concentration of Pb^{2+}.

In the corresponding voltammograms, intriguingly, the Pb striping peak splits into two peaks: peak A centered at -0.56 V which is commonly identified as the Pb peak, and peak B at -0.49 V (Figure 3.4d,e). However, the splitting phenomenon is unobservable in the voltammograms detecting only 80 ppb Pb^{2+} with both the GSH-SPCE and bare SPCE (Figure S3.7). It suggests that peak B is impossible to stem from the interaction of Pb-carbon, Pb-GSH, or Pb-Pb,[46] and the most possibility is therefore caused by the Pb-Cd interaction.

Based on the idea that peak B acts as an indicator to evaluate the interaction of Pb-Cd, the maximum current of peak B was plotted with the corresponding Cd^{2+} concentration in Figure 3.4f (red rectangle for GSH-SPCE, black rectangle for bare SPCE). The much lower values were obtained by the GSH-SPCE compared to the bare SPCE. It proves that GSH assists the bare SPCE to reduce the negative effect from the Pb-Cd interaction.

After investigating the enhancement of Cd^{2+} sensitivity by GSH with the interference of Pb^{2+} or Cu^{2+} separately, then the question was aroused whether GSH can alleviate mutual interference amongst the 3 HMIs (i.e., Cd^{2+}, Pb^{2+}, and Cu^{2+}). Hence, a comparative experiment between GSH-SPCE and bare SPCE was conducted in the mixed solutions containing these 3 HMIs with only one HM varying its concentration and the other two remaining at 80 ppb. In Figure 3.4(g-i), with the interference of Pb^{2+} and Cu^{2+}, the GSH-SPCE significantly increased the Cd^{2+} sensitivity and linearity, compared to the bare SPCE, which on the other hand showed a negligible sensitivity (summarized in Table S3.3). However, regarding the sensitivity of Pb^{2+} and Cu^{2+}, both were minimally influenced by the GSH (Figure 3.4(h, i)).

3.2.7.3   Simultaneous Detection toward Cd^{2+}, Pb^{2+}, and Cu^{2+}

To further understand the simultaneous sensing performances, the GSH-SPCE was examined in the mixed solution containing multi-HMIs of Cd^{2+}, Pb^{2+}, and Cu^{2+} with a fixed ratio of 1:1:1 (Figure 3.5). As a comparison, the bare SPCE was tested under the same condition. The sensitivity of the GSH-SPCE to Cd^{2+} showed a 6-fold enhancement compared to the bare SPCE;

however, the sensitivity of Pb^{2+} and Cu^{2+} was only slightly increased by 1.5 times (Table S3.3). Besides, the bare SPCE had poor linearity to Cd^{2+} (R^2=0.84) due to the influence from Pb^{2+} and Cu^{2+}, while GSH-SPCE was comparatively much better (R^2=0.99). Moreover, a lower LOD of Cd^{2+} (15 ppb) was achieved by the GSH-SPCE than that of the bare SPCE (84 ppb). Regarding Cu^{2+} and Pb^{2+}, the LOD only showed slight improvement by GSH (Table S3.4). All the stripping peaks (Figure 3.5d) were well separated. Amongst them, the peaks at -0.86 V and -0.2 V can be referred to as Cd and Cu respectively, and the peaks around -0.5 V can be identified as Pb.
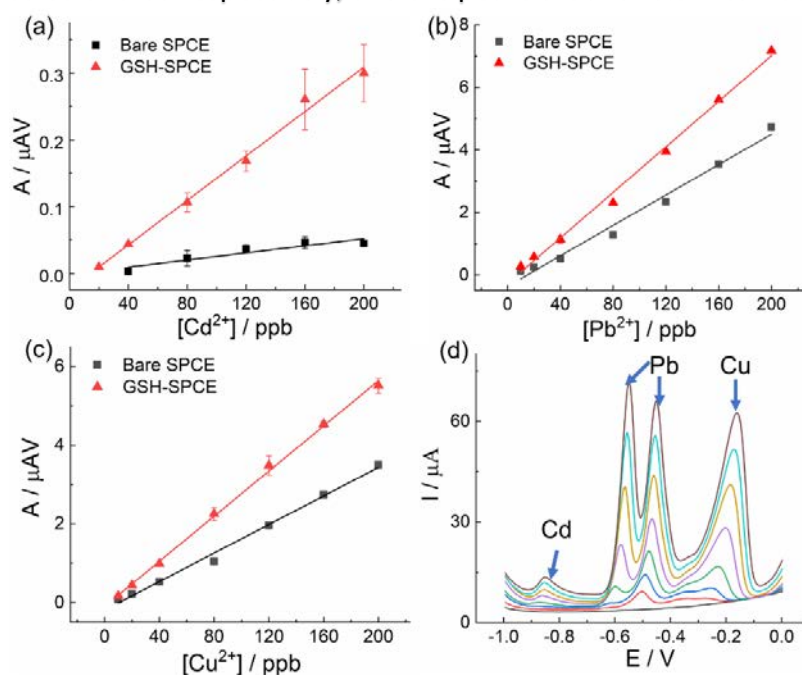

Figure 3.5 The sensing performance of GSH-SPCE and bare SPCE in simultaneous detection of Cd^{2+}, Pb^{2+} and Cu^{2+}. Simultaneous detection in the mixed solution of Cd^{2+}, Pb^{2+} and Cu^{2+} with a fixed ratio of 1:1:1. The calibration curves of GSH-SPCE and bare SPCE in (a) Cd^{2+}, (b) Pb^{2+}, and (c) Cu^{2+}. (d)The voltammograms of GSH-SPCE from blank to 200 ppb of Cd^{2+}, Pb^{2+} and Cu^{2+} (from black to brown).

3.2.7.4   Reusability and Reproducibility

Since the thiol moieties were covalently functionalized, which is believed to be more stable and robust than non-covalent functionalization,[38] the GSH-SPCE would have better stability than the electrodes modified with non-covalently functionalized graphene. Hence, GSH-SPCE was subjected to continuous measurements in the mixed solution of Cd^{2+}, Pb^{2+} and Cu^{2+} ions (with ratio of 1:1:1 at 80 ppb). The repeatability was recorded as 35.7%, 3.7%, and 2.9% for Cd^{2+}, Pb^{2+} and Cu^{2+}, respectively. It should be noticed that the relatively high repeatability toward Cd^{2+} resulted from the highest signals from the first two measurements (Figure S3.8a), which is also typical for the bare SPCE (Figure S3.8b). It may be attributed to the higher availability of active sites on unused SPCE for Cd^{2+}. Evacuating the first two abnormal results, the GSH-SPCE can be reused for 23 cycling times (RSD<20%). The number of usable cycles surpasses other reported studies of non-covalently functionalized graphene sensors.[21,47] It is even better than part of bismuth-based SPCEs (6-12 times).[18,19]

The reproducibility is pivotal for mass production, hence, five GSH-SPCEs and five bare SPCEs were tested in the mixed solution of Cd^{2+}, Pb^{2+}, and Cu^{2+} with the ratio of 1:1:1. All the sensitivities data are shown in Table S3.5. The reproducibility of GSH-SPCE was 17.5%, 5.1%, and 10.9% to Cd^{2+}, Pb^{2+}, and Cu^{2+} respectively.

3.2.7.5 Statical Analysis of GSH Enhancing Cd^{2+} Sensitivity in Simultaneous Detection and the Comparison with Other Graphene Derivatives

To further prove the enhancement of sensitivity by the GSH statistically, Student's t-tests were used to analyze all the sensitivity data obtained in the reproducibility study between Group GSH and Group bare (Figure 3.6a-c). GSH is proved to enhance the sensitivity of bare SPCEs toward Cd^{2+} statistically, with the returned p-value (p=0.0005) below the threshold of a highly significant level (Figure 3.6a).[21] Intriguingly, the sensitivity of Pb^{2+} and Cu^{2+} did not show a significant difference. This finding corroborates the high specific affinity of GSH to Cd^{2+} amongst the three HMIs.
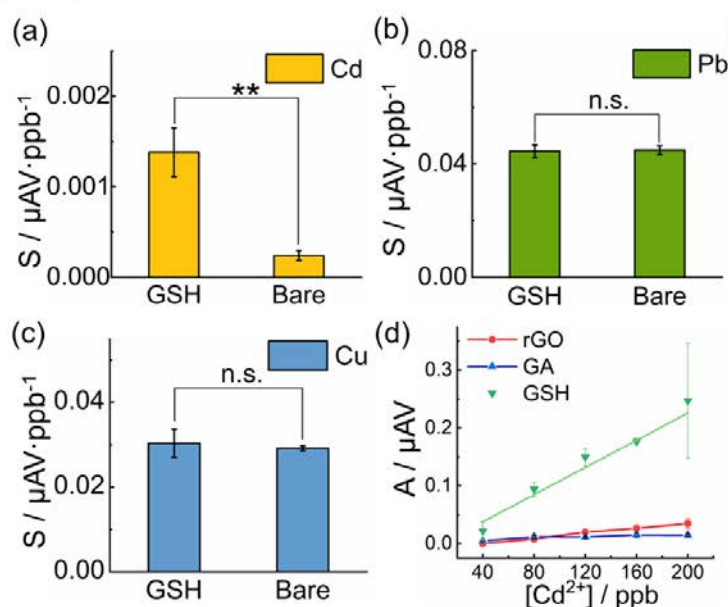

Figure 3.6 Reproducibility study and mechanism discussion. The sensitivity to (a) Cd^{2+}, (b) Pb^{2+}, and (c) Cu^{2+} of different GSH-SPCEs and different bare SPCEs in reproducibility study. (d) The calibration curves of Cd^{2+} in simultaneous detection using the GSH-SPCE with comparison to other graphene derivatives modified SPCEs.

To understand whether the selective enhancement originates from the thiol moieties or graphene sheets, we modified SPCEs with other graphene derivatives as references, *i.e.*, GA and rGO, with carboxyl groups (-COOH) and other oxygen groups, respectively. GA has been characterized in the previous study.[29,30] GO (Angstron Materials, USA) was electrochemically reduced *in situ* on a SPCE after drop casting.[48] However, due to the different hydrophilicity of these graphene derivatives, the supernatants of GA and GO were diluted to secure similar concentrations with the GSH supernatant by UV-Vis *via* Beer-Lambert law (Figure S3.9, ~0.01 mg ml^{-1}). Then, GA and GO followed the same drop casting procedure with GSH to modify

SPCEs. Finally, only GO (on the SPCE) was *in situ* reduced *via* CV and chronometry before being tested in solutions containing HMIs.

The GSH-SPCE showed the best sensitivity toward Cd^{2+} compared to the tests of GA and rGO (after *in-situ* electroreduction) modified SPCEs in the same simultaneous detection toward Cd^{2+}, Pb^{2+}, and Cu^{2+} ions (Figure 3.6d). It indicates the bound thiol moieties, instead of graphene sheets, are reasonable for the high binding affinity of GSH toward Cd^{2+}, and thus alleviating the interference from Pb^{2+} and Cu^{2+}.

According to *Pearson's hard and soft acid and base* (HSAB) theory, this phenomenon can be explained that soft bases (*e.g.*, RSH) have a stronger affinity for soft acids (*e.g.*, Cd^{2+}) rather than hard bases (*e.g.*, RCOOH).[49] Vice versa, Cd^{2+} as a soft acid presents a better affinity to soft bases, like thiols, compared to Pb^{2+} and Cu^{2+} which act as intermediate acids (summarized in Table 3.1).[50] Therefore, the free thiol groups in GSH provide potent coordination sites for Cd^{2+}, increasing the concentration of Cd^{2+} on the electrode surface even under the interference of Pb^{2+} and Cu^{2+}.

Table 3.1 Typical hard and soft acids and bases examples [50]

Hard acids	H^+, Na^+, K^+, Mg^{2+}, Ca^{2+}
Hard bases	RNH_2, ROH, RCOOH
Soft acids	Cd^{2+}, Hg^{2+}, Pt^{2+}, Pd^{2+}
Soft bases	R_2S, RSH, RS^-
Intermediate acids	Pb^{2+}, Cu^{2+}, Zn^{2+}, Fe^{2+}, Ni^{2+}
Intermediate bases	$C_6H_5NH_2$

Moreover, the defects in the GSH nanosheets structures (as can be seen in the relatively high I_D/I_G in Figure S2) could provide active binding sites for HMIs on graphene backbones, which induce less competition and renders the deposition of Cd^{2+} more feasibly on the surface of the electrode.[51]

3.2.8   Interference Study of GSH-SPCE and Its Validation in Real Sample

To mimic the real sample, the interference of other ions (*i.e.*, Na^+, K^+, Ca^{2+}, Mg^{2+}, Ni^{2+}, Zn^{2+}, As^{3+}, Hg^{2+} with the 5-fold concentration of Cd^{2+}, Pb^{2+}, and Cu^{2+}) was studied using the GSH-SPCE. The responses of Cd^{2+}, Pb^{2+}, and Cu^{2+} decreased to 74%, 97%, and 89%, respectively, compared with those without interference. The signal loss of Cd^{2+} could be caused by Hg^{2+}, which is also a soft acid competing for the thiol active sites. (Figure S3.10)

GSH-SPCE was then validated in tap water with spiked HMs (Cd:Pb: Cu=1:1:1) from 10 ppb to 200 ppb (Figure S3.11) The obtained sensitivity values of Cd^{2+}, Pb^{2+}, and Cu^{2+} in tap water were similar to the ones in standard solutions (Table S3.3). Afterward, a recovery/accuracy test was conducted by the GSH-SPCE in a spiked solution of 90 ppb of Cd^{2+}, Pb^{2+}, and Cu^{2+} with

the same tap water. All the recoveries were approximately 80% (shown in Table S3.6), whereby the data from the gold standard method (ICP-MS) were shown as reference.

3.2.9   Comparison with Other Studies

Lastly, the GSH-SPCE was compared with the presented studies shown in Table 3.7. Although the LOD of the GSH-SPCE (15 ppb, 11 ppb, and 6 ppb for Cd^{2+}, Pb^{2+}, and Cu^{2+}, respectively) is not as low as some sub-ppb level LOD obtained by GCEs, or by the bismuth-based SPCEs, there are several advantages of the GSH-SPCE.

Table 3.7 Comparison with other studies.

Functional materials	Electrodes	Cd Sensitivity	Cd LOD (ppb)	Pb Sensitivity	Pb LOD (ppb)	Cu Sensitivity	Cu LOD (ppb)	Metal - free	Detection type	REF
Glutathione	SPCE	0.63 (AV/ppb)	3.20	3.02 (AV/ppb)	3.00	-	-	yes	Individual	20
DTT/GO/Nafion	SPCE	-	8.00	-	2.20 ppb	-	0.50	yes	Simultaneous	21
Cysteine-GO/Ppy	SPCE	-	-	0.011 (µA/ppb)	0.070	-	-	yes	Individual	47
Graphene	Laser-scribed PI	-	-	-	15.00	-	-	yes	Individual	52
MoS_2/rGO	GCE	-	-	42.91 (µA/µM)	1.04	-	-	yes	Individual	53
Poly (L-glutamic acid)/GO	GCE	7.29 (µA/µM)	1.68	-	-	8.95 (µA/µM)	1.52	yes	Simultaneous	54
Thiol-CNTs	GCE	0.53 (µA/ppb)	0.40	0.36 (µA/ppb)	0.30	-	-	yes	Simultaneous	55
Graphene/polyaniline/polystyrene	SPCE	1.23 (µA/ppb)	4.43	0.73 (µA/ppb)	3.30	-	-	No, 900 ppb of Bi^{2+}	Simultaneous	56
rGO/L-Cysteine	SPCE	0.65 (µA/ppb)	0.10	0.50 (µA/ppb)	0.080	-	-	No, 2000 ppb of Bi^{2+}	Simultaneous	57
GSH	SPCE	0.0017 (µAV/ppb)	15.28	0.036 (µAV/ppb)	10.62	0.027 (µAV/ppb)	6.37	yes	Simultaneous	This study
GSH	SPCE	0.032 (µAV/ppb)	3.36	0.021 (µAV/ppb)	3.49	0.021 (µAV/ppb)	3.61	yes	Individual	This study

First, the metal-free GSH-SPCE is considerably more sustainable and economical to alleviate mutual interference with more reusable cycles compared to the most used bismuth-based SPCEs. Especially, the material used for the synthesis of GSH, namely, graphite fluoride (GF) is a cheap industrial solid lubricant. The synthesis of GSH is in a mass-productive way owing to wet-chemical synthesis, which is suitable to modify the largely manufactured SPCEs.

Moreover, the covalent bond (between amino groups in cysteamine and carbon atoms on the graphene surface) provides GSH extremely high stability in acidic solutions during testing. These moieties on the graphene surface were able to withstand large negative potential without degradation. Reusable times (23 times) in continuous measurement is highlighted for it surpasses other studies using non-covalently functionalized graphene[21,47] and part of bismuth modified SPCEs (6-12 times).[18,19]

Additionally, our testing system can perform *in-situ* and automatic measurements with the assistance of the FSS reported in Chapter 1, allowing a scenario of monitoring drinking water quality at home. In the future, the SPCEs modified with various moieties can be achieved *via* our approach utilizing the covalent interaction between the amines of versatile molecules and GF. It can be highly useful to design new graphene derivatives with specific moieties according to their specific high binding affinity to certain HM pollutants under mutual interference.

3.4   Conclusion

A sustainable approach to alleviating mutual interference was presented using a novel graphene derivative that was covalently functionalized with cysteamine molecules (free thiol groups). GSH proved to boost the diminished sensitivity of the bare SPCE to Cd^{2+} from other target HM ions. In comparison to other graphene derivatives (GA, and rGO), GSH demonstrates the best Cd^{2+} sensitivity, denoting that the free thiol groups are reasonable for the good affinity toward Cd^{2+}. This phenomenon matches the HSAB theory. In multi-HMs detection, GSH-SPCE can detect Cd^{2+}, Pb^{2+}, and Cu^{2+} up to 15 ppb, 11 ppb, and 6 ppb, respectively. The high reusable times (23 times) owing to the covalent functionalization mode, outperformed the state-of-the-art SPCEs based on non-covalent functionalization routes. Importantly, GSH-SPCE offers a metal-free and cost-effective platform with the compatibility of mass production. The versatile functionalization with other chemical groups can be designed to construct selective electrodes, targeting different analytes in the future.

Reference

(1) Csuros, M. *Environmental Sampling and Analysis for Technicians*, 1st Editio.; CRC Press, 1994. https://doi.org/https://doi.org/10.1201/9780203756867.

(2) Aragay, G.; Pons, J.; Merkoçi, A. Recent Trends in Macro-, Micro-, and Nanomaterial-Based Tools and Strategies for Heavy-Metal Detection. *Chem. Rev.* **2011**, *111* (5), 3433–3458. https://doi.org/10.1021/cr100383r.

(3) List of chemicals for Water Framework Directive assessments https://www.gov.uk/government/publications/list-of-chemicals-for-water-framework-directive-assessments.

(4) Schwarzenbach, R. P.; Escher, B. I.; Fenner, K.; Hofstetter, T. B.; Johnson, C. A.; von Gunten, U.; Wehrli, B. The Challenge of Micropollutants in Aquatic Systems. *Science (80-.).* **2006**, *313* (5790), 1072 LP – 1077. https://doi.org/10.1126/science.1127291.

(5) Jomova, K.; Valko, M. Advances in Metal-Induced Oxidative Stress and Human Disease. *Toxicology* **2011**, *283* (2), 65–87. https://doi.org/https://doi.org/10.1016/j.tox.2011.03.001.

(6) Osteryoung, J. G.; Osteryoung, R. A. Square Wave Voltammetry. *Anal. Chem.* **1985**, *57* (1), 1–6. https://doi.org/10.1021/ac00279a789.

(7) Mirceski, V.; Skrzypek, S.; Stojanov, L. Square-Wave Voltammetry. *ChemTexts* **2018**, *4* (4), 1–14. https://doi.org/10.1007/s40828-018-0073-0.

(8) Xu, K.; Clara, P.; Marchoud, A.; Crespo, A. Anodic Stripping Voltammetry with the Hanging Mercury Drop Electrode for Trace Metal Detection in Soil Samples. **2021**.

(9) Honeychurch, K. C.; Hart, J. P. Screen-Printed Electrochemical Sensors for Monitoring Metal Pollutants. *TrAC - Trends Anal. Chem.* **2003**, *22* (7), 456–469. https://doi.org/10.1016/S0165-9936(03)00703-9.

(10) Cadevall, M.; Ros, J.; Merkoçi, A. Bismuth Nanoparticles Integration into Heavy Metal Electrochemical Stripping Sensor. *Electrophoresis* **2015**, *36* (16), 1872–1879. https://doi.org/10.1002/elps.201400609.

(11) Borrill, A. J.; Reily, N. E.; Macpherson, J. V. Addressing the Practicalities of Anodic Stripping Voltammetry for Heavy Metal Detection: A Tutorial Review. *Analyst* **2019**, *144* (23), 6834–6849. https://doi.org/10.1039/c9an01437c.

(12) Huangfu, C.; Fu, L.; Li, Y.; Li, X.; Du, H.; Ye, J. Sensitive Stripping Determination of Cadmium(Ii) and Lead(Ii) on Disposable Graphene Modified Screen-Printed Electrode. *Electroanalysis* **2013**, *25* (9), 2238–2243. https://doi.org/10.1002/elan.201300239.

(13) Xiong, S.; Yang, B.; Cai, D.; Qiu, G.; Wu, Z. Individual and Simultaneous Stripping Voltammetric and Mutual Interference Analysis of Cd2+, Pb2+ and Hg2+ with Reduced Graphene Oxide-Fe3O4 Nanocomposites. *Electrochim. Acta* **2015**, *185*, 52–61. https://doi.org/10.1016/j.electacta.2015.10.114.

(14) Wei, Y.; Yang, R.; Chen, X.; Wang, L.; Liu, J. H.; Huang, X. J. A Cation Trap for Anodic Stripping Voltammetry: NH3-Plasma Treated Carbon Nanotubes for Adsorption and Detection of Metal Ions. *Anal. Chim. Acta* **2012**, *755*, 54–61. https://doi.org/10.1016/j.aca.2012.10.021.

(15) Toghill, K. E.; Xiao, L.; Wildgoose, G. G.; Compton, R. G. Electroanalytical Determination of Cadmium(II) and Lead(II) Using an Antimony Nanoparticle Modified Boron-Doped Diamond Electrode. *Electroanalysis* **2009**, *21* (10), 1113–1118. https://doi.org/10.1002/elan.200904547.

(16) Palchetti, I.; Cagnini, A.; Mascini, M.; Turner, A. P. F. Characterisation of Screen-Printed Electrodes for Detection of Heavy Metals. *Mikrochim. Acta* **1999**, *131* (1–2), 65–73. https://doi.org/10.1007/s006040050010.

(17) Hwang, J.-H.; Wang, X.; Zhao, D.; Rex, M. M.; Cho, H. J.; Lee, W. H. A Novel Nanoporous Bismuth Electrode Sensor for in Situ Heavy Metal Detection. *Electrochim. Acta* **2019**, *298*, 440–448. https://doi.org/https://doi.org/10.1016/j.electacta.2018.12.122.

(18) Hočevar, S. B.; Švancara, I.; Vytřas, K.; Ogorevc, B. Novel Electrode for Electrochemical Stripping Analysis Based on Carbon Paste Modified with Bismuth Powder. *Electrochim. Acta* **2005**, *51* (4), 706–710. https://doi.org/https://doi.org/10.1016/j.electacta.2005.05.023.

(19) Sahoo, P. K.; Panigrahy, B.; Sahoo, S.; Satpati, A. K.; Li, D.; Bahadur, D. In Situ Synthesis and Properties of Reduced Graphene Oxide/Bi Nanocomposites: As an Electroactive Material for Analysis of Heavy Metals. *Biosens. Bioelectron.* **2013**, *43*, 293–296. https://doi.org/https://doi.org/10.1016/j.bios.2012.12.031.

(20)   Pérez-Ràfols, C.; Serrano, N.; Díaz-Cruz, J. M.; Ariño, C.; Esteban, M. Glutathione Modified Screen-Printed Carbon Nanofiber Electrode for the Voltammetric Determination of Metal Ions in Natural Samples. *Talanta* **2016**, *155*, 8–13. https://doi.org/10.1016/j.talanta.2016.04.011.

(21)   Choi, S. M.; Kim, D. M.; Jung, O. S.; Shim, Y. B. A Disposable Chronocoulometric Sensor for Heavy Metal Ions Using a Diaminoterthiophene-Modified Electrode Doped with Graphene Oxide. *Anal. Chim. Acta* **2015**, *892*, 77–84. https://doi.org/10.1016/j.aca.2015.08.037.

(22)   Malhotra, M.; Puglia, M.; Kalluri, A.; Chowdhury, D.; Kumar, C. V. Adsorption of Metal Ions on Graphene Sheet for Applications in Environmental Sensing and Wastewater Treatment. *Sensors and Actuators Reports* **2022**, 100077. https://doi.org/https://doi.org/10.1016/j.snr.2022.100077.

(23)   Georgakilas, V.; Otyepka, M.; Bourlinos, A. B.; Chandra, V.; Kim, N.; Kemp, K. C.; Hobza, P.; Zboril, R.; Kim, K. S. Functionalization of Graphene: Covalent and Non-Covalent Approaches, Derivatives and Applications. *Chem. Rev.* **2012**, *112* (11), 6156–6214. https://doi.org/10.1021/cr3000412.

(24)   Béraud, A.; Sauvage, M.; Bazán, C. M.; Tie, M.; Bencherif, A.; Bouilly, D. Graphene Field-Effect Transistors as Bioanalytical Sensors: Design, Operation and Performance. *Analyst* **2021**, *146* (2), 403–428. https://doi.org/10.1039/d0an01661f.

(25)   Liu, Y.; Zhou, J.; Zhang, X.; Liu, Z.; Wan, X.; Tian, J.; Wang, T.; Chen, Y. Synthesis, Characterization and Optical Limiting Property of Covalently Oligothiophene-Functionalized Graphene Material. *Carbon N. Y.* **2009**, *47* (13), 3113–3121. https://doi.org/https://doi.org/10.1016/j.carbon.2009.07.027.

(26)   Gilje, S.; Dubin, S.; Badakhshan, A.; Farrar, J.; Danczyk, S. A.; Kaner, R. B. Photothermal Deoxygenation of Graphene Oxide for Patterning and Distributed Ignition Applications. *Adv. Mater.* **2010**, *22* (3), 419–423. https://doi.org/https://doi.org/10.1002/adma.200901902.

(27)   Matochová, D.; Medveď, M.; Bakandritsos, A.; Steklý, T.; Zbořil, R.; Otyepka, M. 2D Chemistry: Chemical Control of Graphene Derivatization. *J. Phys. Chem. Lett.* **2018**, *9* (13), 3580–3585. https://doi.org/10.1021/acs.jpclett.8b01596.

(28)   Medveď, M.; Zoppellaro, G.; Ugolotti, J.; Matochová, D.; Lazar, P.; Pospíšil, T.; Bakandritsos, A.; Tuček, J.; Zbořil, R.; Otyepka, M. Reactivity of Fluorographene Is Triggered by Point Defects: Beyond the Perfect 2D World. *Nanoscale* **2018**, *10* (10), 4696–4707. https://doi.org/10.1039/C7NR09426D.

(29)   Bakandritsos, A.; Pykal, M.; Boński, P.; Jakubec, P.; Chronopoulos, D. D.; Poláková, K.; Georgakilas, V.; Čépe, K.; Tomanec, O.; Ranc, V.; Bourlinos, A. B.; Zbořil, R.; Otyepka, M. Cyanographene and Graphene Acid: Emerging Derivatives Enabling High-Yield and Selective Functionalization of Graphene. *ACS Nano* **2017**, *11* (3), 2982–2991. https://doi.org/10.1021/acsnano.6b08449.

(30)   Šedajová, V.; Jakubec, P.; Bakandritsos, A.; Ranc, V.; Otyepka, M. New Limits for Stability of Supercapacitor Electrode Material Based on Graphene Derivative. *Nanomaterials* **2020**, *10* (9). https://doi.org/10.3390/nano10091731.

(31)   Flauzino, J. M. R.; Nguyen, E. P.; Yang, Q.; Rosati, G.; Panáček, D.; Brito-Madurro, A. G.; Madurro, J. M.; Bakandritsos, A.; Otyepka, M.; Merkoçi, A. Label-Free and Reagentless Electrochemical Genosensor Based on Graphene Acid for Meat Adulteration Detection. *Biosens. & Bioelectron.* **2022**, *195*, 113628. https://doi.org/10.1016/j.bios.2021.113628.

(32)   Bakandritsos, A.; Kadam, R. G.; Kumar, P.; Zoppellaro, G.; Medved', M.; Tuček, J.; Montini, T.; Tomanec, O.; Andrýsková, P.; Drahoš, B.; Varma, R. S.; Otyepka, M.; Gawande, M. B.; Fornasiero, P.; Zbořil, R. Mixed-Valence Single-Atom Catalyst Derived from Functionalized Graphene. *Adv. Mater.* **2019**, *31* (17), 1900323. https://doi.org/https://doi.org/10.1002/adma.201900323.

(33)   Henderson, W. A.; Schultz, C. J. The Nucleophilicity of Amines. *J. Org. Chem.* **1962**, *27* (12), 4643–4646. https://doi.org/10.1021/jo01059a507.

(34)   Yang, Q.; Nagar, B.; Alvarez-Diduk, R.; Balsells, M.; Farinelli, A.; Bloisi, D.; Proia, L.; Espinosa, C.; Ordeix, M.; Knutz, T.; De Vito-Francesco, E.; Allabashi, R.; Merkoçi, A. Development of a Heavy Metal Sensing Boat for Automatic Analysis in Natural Waters Utilizing Anodic Stripping Voltammetry. *ACS ES&T Water* **2021**. https://doi.org/10.1021/acsestwater.1c00192.

(35)   Shang, J.; Xue, F.; Ding, E. The Facile Fabrication of Few-Layer Graphene and Graphite Nanosheets by High Pressure Homogenization. *Chem. Commun.* **2015**, *51* (87), 15811–15814. https://doi.org/10.1039/C5CC06151B.

(36)   Abdulla, M.; Ali, A.; Jamal, R.; Bakri, T.; Wu, W.; Abdiryim, T. Electrochemical Sensor of Double-Thiol Linked PProDOT@Si Composite for Simultaneous Detection of Cd(II), Pb(II), and Hg(II). *Polymers (Basel).* **2019**, *11* (5), 1–19. https://doi.org/10.3390/polym11050815.

(37)   Chronopoulos, D. D.; Bakandritsos, A.; Pykal, M.; Zbořil, R.; Otyepka, M. Chemistry, Properties, and Applications of Fluorographene. *Appl. Mater. Today* **2017**, *9*, 60–70. https://doi.org/10.1016/j.apmt.2017.05.004.

(38)   Vermisoglou, E. C.; Jakubec, P.; Bakandritsos, A.; Kupka, V.; Pykal, M.; Šedajová, V.; Vlček, J.; Tomanec, O.; Scheibe, M.; Zbořil, R.; Otyepka, M. Graphene with Covalently Grafted Amino Acid as a Route Toward Eco-Friendly and Sustainable Supercapacitors. *ChemSusChem* **2021**, *14* (18), 3904–3914. https://doi.org/https://doi.org/10.1002/cssc.202101039.

(39)   Tantis, I.; Bakandritsos, A.; Zaoralová, D.; Medveď, M.; Jakubec, P.; Havláková, J.; Zbořil, R.; Otyepka, M. Covalently Interlinked Graphene Sheets with Sulfur-Chains Enable Superior Lithium–Sulfur Battery Cathodes at Full-Mass Level. *Adv. Funct. Mater.* **2021**, *31* (30), 2101326. https://doi.org/https://doi.org/10.1002/adfm.202101326.

(40)   Zhang, S. Sulfurized Carbon: A Class of Cathode Materials for High Performance Lithium/Sulfur Batteries. *Front. Energy Res.* **2013**, *1*, 10. https://doi.org/10.3389/fenrg.2013.00010.

(41)   Mishra, A.; Jha, B. Isolation and Characterization of Extracellular Polymeric Substances from Micro-Algae Dunaliella Salina under Salt Stress. *Bioresour. Technol.* **2009**, *100* (13), 3382–3386. https://doi.org/https://doi.org/10.1016/j.biortech.2009.02.006.

(42)   Ahn, M.; Liu, R.; Lee, C.; Lee, W. Designing Carbon/Oxygen Ratios of Graphene Oxide Membranes for Proton Exchange Membrane Fuel Cells. *J. Nanomater.* **2019**, *2019*, 6464713. https://doi.org/10.1155/2019/6464713.

(43)   Ulman, A.; Ioffe, M.; Patolsky, F.; Haas, E.; Reuvenov, D. Highly Active Engineered-Enzyme Oriented Monolayers: Formation, Characterization and Sensing Applications. *J. Nanobiotechnology* **2011**, *9* (1), 26. https://doi.org/10.1186/1477-3155-9-26.

(44)   Zhao, G.; Tong, X.; Hu, Z.; Xiao, X.; Li, D. Electrochemical Costripping Models and Mutual Interferences of Mutli-Transition Metal Systems on the Surface of Boron-Doped Diamond. *Electrochim. Acta* **2008**, *53* (12), 4283–4292. https://doi.org/10.1016/j.electacta.2008.01.017.

(45)   Zhai, Z.; Huang, N.; Zhuang, H.; Liu, L.; Yang, B.; Wang, C.; Gai, Z.; Guo, F.; Li, Z.; Jiang, X. A Diamond/Graphite Nanoplatelets Electrode for Anodic Stripping Voltammetric Trace Determination of Zn(II), Cd(II), Pb(II) and Cu(II). *Appl. Surf. Sci.* **2018**, *457* (June), 1192–1201. https://doi.org/10.1016/j.apsusc.2018.06.266.

(46)   Honeychurch, K. C.; Hart, J. P.; Cowell, D. C. Voltammetric Behavior and Trace Determination of Lead at a Mercury-Free Screen-Printed Carbon Electrode. *Electroanalysis* **2000**, *12* (3), 171–177. https://doi.org/https://doi.org/10.1002/(SICI)1521-4109(200002)12:3<171::AID-ELAN171>3.0.CO;2-Q.

(47)   Seenivasan, R.; Chang, W. J.; Gunasekaran, S. Highly Sensitive Detection and Removal of Lead Ions in Water Using Cysteine-Functionalized Graphene Oxide/Polypyrrole Nanocomposite Film Electrode. *ACS Appl. Mater. Interfaces* **2015**, *7* (29), 15935–15943. https://doi.org/10.1021/acsami.5b03904.

(48)   Kudr, J.; Zhao, L.; Nguyen, E. P.; Arola, H.; Nevanen, T. K.; Adam, V.; Zitka, O.; Merkoçi, A. Inkjet-Printed Electrochemically Reduced Graphene Oxide Microelectrode as a Platform for HT-2 Mycotoxin Immunoenzymatic Biosensing. *Biosens. Bioelectron.* **2020**, *156*, 112109. https://doi.org/https://doi.org/10.1016/j.bios.2020.112109.

(49)   Ho, T.-L. Hard Soft Acids Bases (HSAB) Principle and Organic Chemistry. *Chem. Rev.* **1975**, *75* (1), 1–20. https://doi.org/10.1021/cr60293a001.

(50)   Bjørklund, G.; Crisponi, G.; Nurchi, V. M.; Cappai, R.; Djordjevic, A. B.; Aaseth, J. A Review on Coordination Properties of Thiol-Containing Chelating Agents towards Mercury, Cadmium, and Lead. *Molecules* **2019**, *24* (18), 1–32. https://doi.org/10.3390/molecules24183247.

(51)   Ambrosi, A.; Chua, C. K.; Bonanni, A.; Pumera, M. Electrochemistry of Graphene and Related Materials. *Chem. Rev.* **2014**, *114* (14), 7150–7188. https://doi.org/10.1021/cr500023c.

(52)   Getachew, B. A.; Bergsman, D. S.; Grossman, J. C. Laser-Induced Graphene from Polyimide and Polyethersulfone Precursors as a Sensing Electrode in Anodic Stripping Voltammetry. *ACS Appl. Mater. Interfaces* **2020**, *12* (43), 48511–48517. https://doi.org/10.1021/acsami.0c11725.

(53)   Sun, Y.-F.; Sun, J.-H.; Wang, J.; Pi, Z.-X.; Wang, L.-C.; Yang, M.; Huang, X.-J. Sensitive and Anti-Interference Stripping Voltammetry Analysis of Pb(II) in Water Using Flower-like MoS2/RGO Composite with Ultra-Thin Nanosheets. *Anal. Chim. Acta* **2019**, *1063*, 64–74. https://doi.org/https://doi.org/10.1016/j.aca.2019.03.008.

(54)   Yi, W.; He, Z.; Fei, J.; He, X. Sensitive Electrochemical Sensor Based on Poly(l-Glutamic Acid)/Graphene Oxide Composite Material for Simultaneous Detection of Heavy Metal Ions. *RSC Adv.* **2019**, *9* (30), 17325–17334. https://doi.org/10.1039/C9RA01891C.

(55)   Li, X.; Zhou, H.; Fu, C.; Wang, F.; Ding, Y.; Kuang, Y. A Novel Design of Engineered Multi-Walled Carbon Nanotubes Material and Its Improved Performance in Simultaneous Detection of Cd(II) and Pb(II) by Square Wave Anodic Stripping Voltammetry. *Sensors Actuators, B Chem.* **2016**, *236*, 144–152. https://doi.org/10.1016/j.snb.2016.05.149.

(56)   Promphet, N.; Rattanarat, P.; Rangkupan, R.; Chailapakul, O.; Rodthongkum, N. An Electrochemical Sensor Based on Graphene/Polyaniline/Polystyrene Nanoporous Fibers Modified Electrode for Simultaneous Determination of Lead and Cadmium. *Sensors Actuators, B Chem.* **2015**, *207* (PartA), 526–534. https://doi.org/10.1016/j.snb.2014.10.126.

(57)   Hou, X.; Xiong, B.; Wang, Y.; Wang, L.; Wang, H. Determination of Trace Lead and Cadmium in Decorative Material Using Disposable Screen-Printed Electrode Electrically Modified with Reduced Graphene Oxide/L-Cysteine/Bi-Film. *Sensors* **2020**, *20* (5). https://doi.org/10.3390/s20051322.

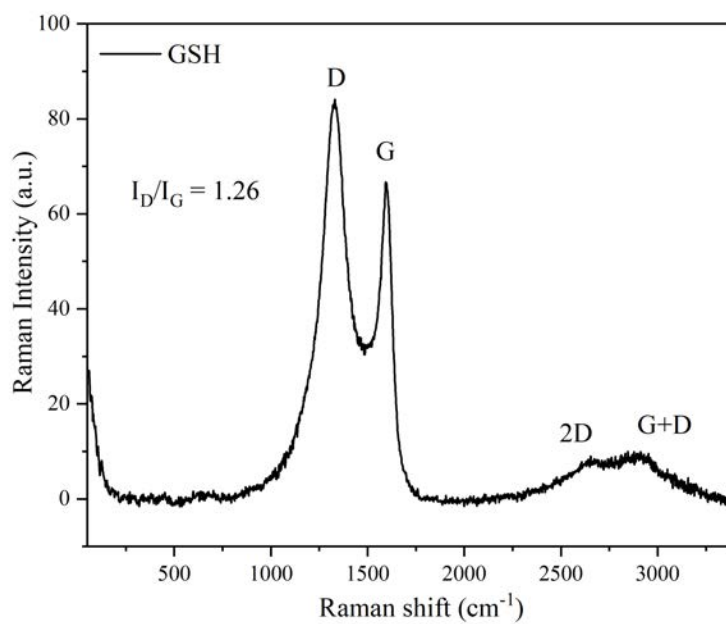# Supporting Information

Raman Characterization

Figure S3.1: Raman spectrum of GSH nanosheet

Optimization of GSH-SPCE Testing Conditions

The type of supporting electrolyte and its concentration, flow rate, flow time, and deposition time were optimized. Each of them and the amount of GSH added to the devices have been optimized with a one-variable at a time approach.
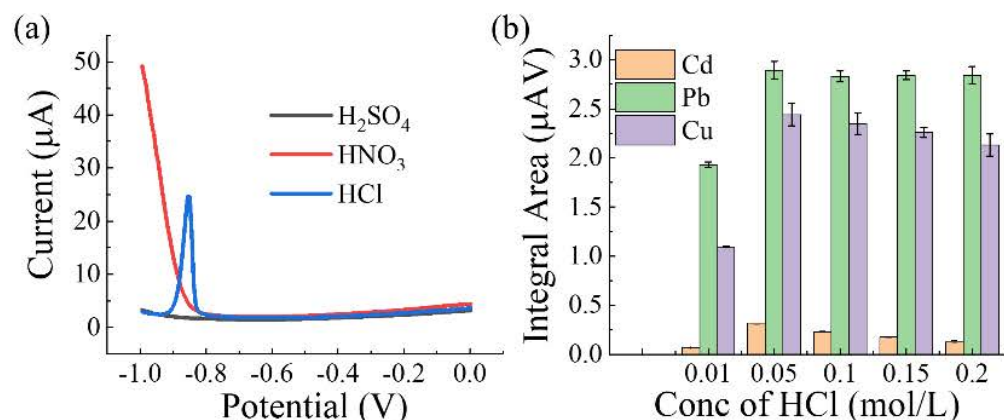

Figure S3.2 Optimization of different supporting electrolytes and concentrations (a) The GSH-SPCE voltammogram of 80 ppb Cd in the different supporting electrolytes of 0.05 M HCl, 0.05 M HNO$_3$ and 0.025 M H$_2$SO$_4$. (b) GSH-SPCE were tested in 80 ppb Cd^{2+}, Pb^{2+} and Cu^{2+} with various concentrations of HCl (0.01, 0.05, 0.1, 0.15 and 0.2 M). 0.05 M HCl was selected for the best performance.
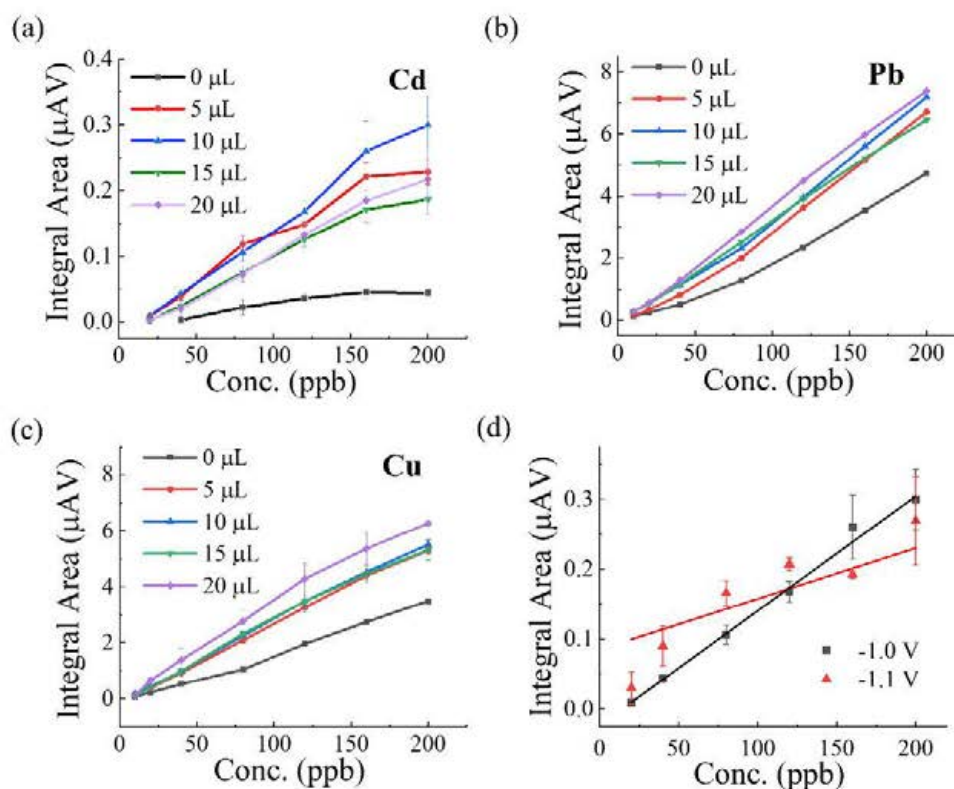

Figure S3.3 Optimization of different volume of GSH supernatant drop-casted on SPCEs and deposition potential. GSH-SPCE with different GSH volumes were tested in various concentrations of Cd^{2+}, Pb^{2+} and Cu^{2+} (1:1:1) in 0.05 M HCl. The tested signals with varied HM concentrations of (a) Cd^{2+}, (b) Pb^{2+} and (c) Cu^{2+}. The sensitivities/slopes of Cd from 0 to 20 μL

were 0.0003, 0.0013, 0.0017, 0.0011, and 0.0012 μAV·ppb^{-1}, respectively. The sensitivities of Pb from 0 to 20 μL were 0.024, 0.035, 0.036, 0.033, and 0.0381 μAV·ppb^{-1}, respectively. The sensitivities of Cu from 0 to 20 μL were 0.018, 0.028, 0.029, 0.028, and 0.033 μAV·ppb^{-1}, respectively. 10 μL was selected for the best Cd signals. (d) The calibration curve of Cd in a mixed solution of Cd^{2+}, Pb^{2+}, and Cu^{2+} (remaining a fixed ratio of 1:1:1) with different deposition potentials (-1 V and -1.1 V). -0.9 V has been tested as depositing potential but is not drawn in the plots, for there are no observable Cd signals.

Table S3.1 The detailed data in optimization of different deposition potentials. Detailed sensitivity and R-square of Cd^{2+}, Pb^{2+}, and Cu^{2+} in the calibration during different deposition potentials of -1 V and -1.1 V. 1.0 V was selected for better slope and linearity. -0.9 V was imposed on the working electrode as deposition potential, too. However, no Cd signal was observed, and thus -0.9 V was discarded.

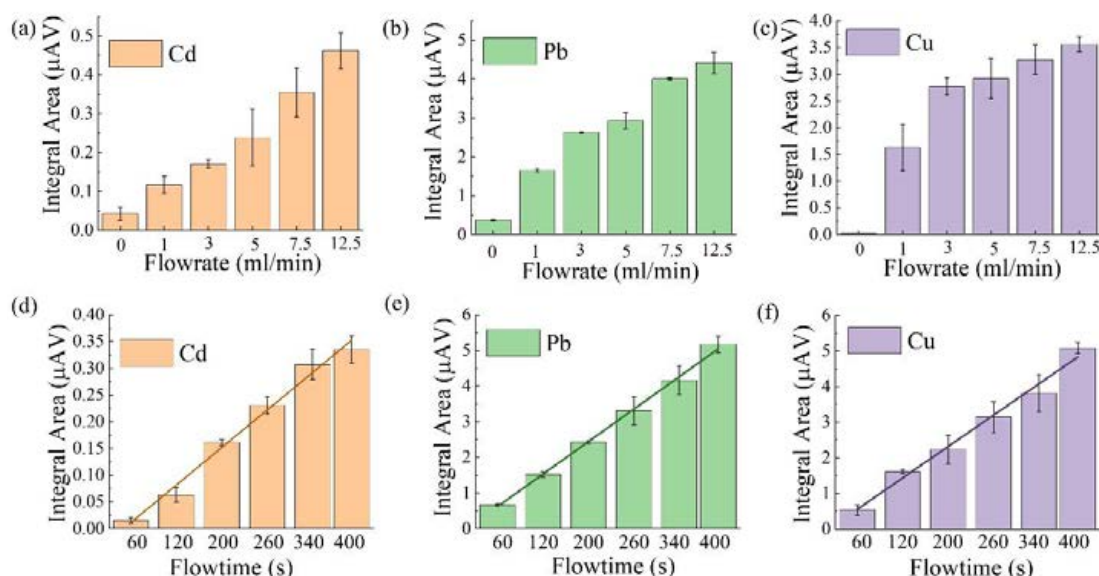|		-1.0 V	-1.1 V
Cd	Slope	0.0017	0.0012
	R^2	0.993	0.8888
Pb	Slope	0.0364	0.0369
	R^2	0.9951	0.9716
Cu	Slope	0.0287	0.0264
	R^2	0.9982	0.9755

Figure S3.4. Optimization of flow time and flow rate. The GSH-SPCE signal diagram of (a) Cd, (b) Pb, and (c) Cu in the mixed 80ppb Cd^{2+}, 80ppb Pb^{2+} and 80ppb Cu^{2+} solution with different flow rate. 3 mL min^{-1} was selected for Pb and Cu signals not increasing much with a higher flow rate. The GSH-SPCE signal diagram of (d) Cd^{2+}, (e) Pb^{2+}, and (f) Cu^{2+} in the mixed 80ppb

Cd^{2+}, 80ppb Pb^{2+} and 80ppb Cu^{2+} solution with different flow time (deposition time). 200s was selected for a mediate sensing signal with rapid sensing time.

Calibrations of Cd^{2+}, Pb^{2+} And Cu^{2+} in Their Individual Solutions
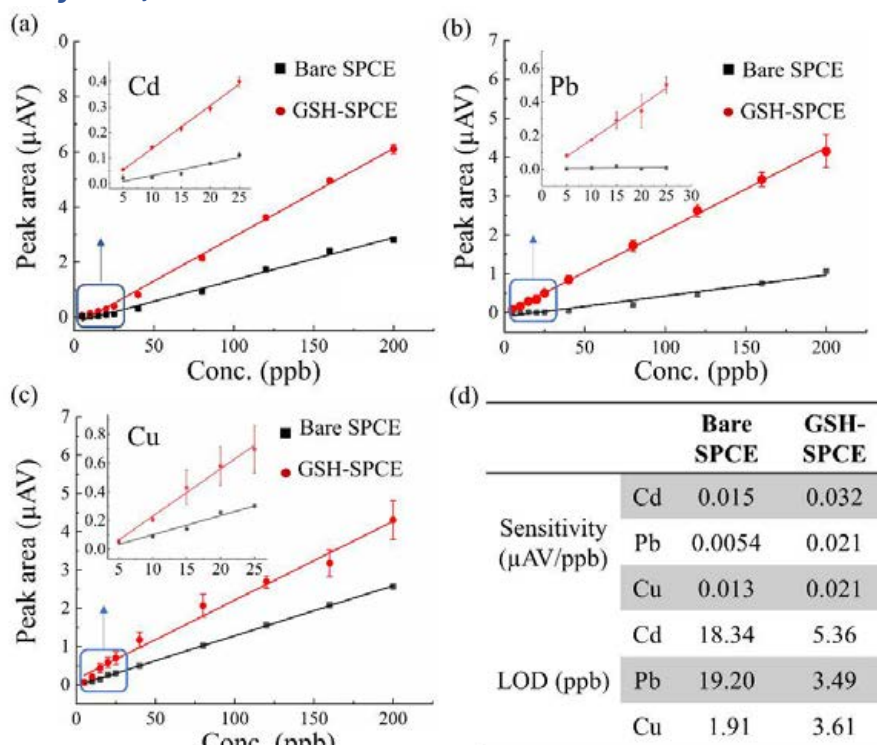

Figure S3.5 The individual HMIs detection. The calibration curves to (a) Cd^{2+}, (b) Pb^{2+} and (c) Cu^{2+} of GSH-SPCE (red) and bare SPCE (black). (d) The detailed sensitivity and LOD in bare SPCE and GSH-SPCE.

CV and EIS Characterizations of GSH-SPCE and Bare SPCE

The GSH-SPCE and bare SPCE were used to perform CV and EIS with a standard potentiostat (PGSTAT12, Autolab) in 10 mM Ferro/Ferricyanide in 0.1 M KCl. The SPCEs were tested by EIS with the applied potential of E^0. The measurements were performed in the 1 Hz-10 kHz frequency range, 10 points per decade. EIS data were fit with the Randle equivalent circuit using Zview 2® software (Scribner and Associates).
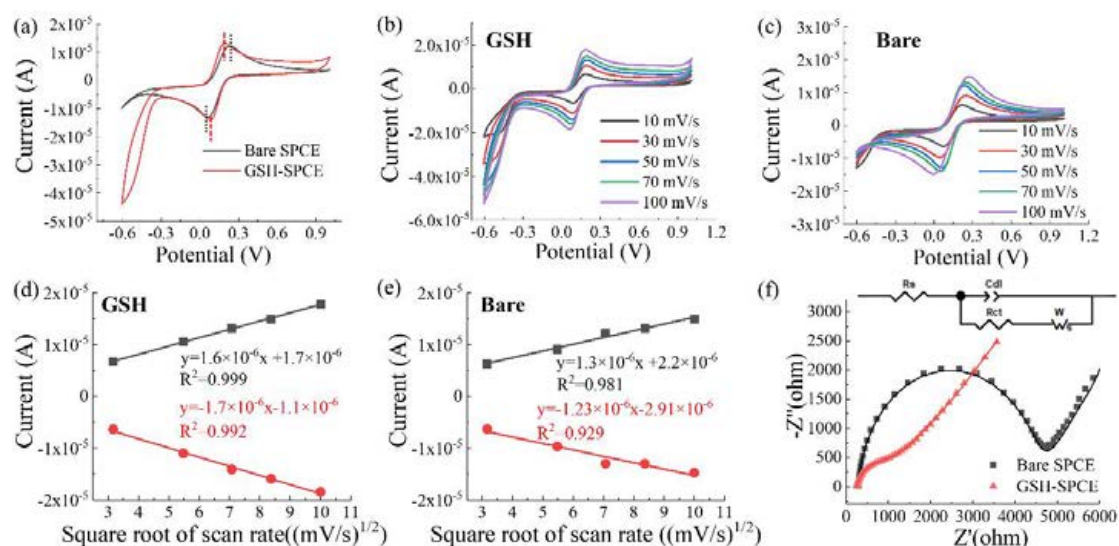

Figure S3.6 Cyclic voltammetry and electrochemical impedance spectroscopy of Bare and GSH-SPCE. (a) Cyclic voltammetry (CV) of GSH-SPCE and bare SPCE in 0.01 M $[Fe(CN)_6]^{4-/3-}$ in 0.1 M KCl at the scan rate of 50 mV/s. Cyclic voltammetry of (b) GSH-SPCE and (c) bare SPCE in 0.01 M $[Fe(CN)_6]^{4-/3-}$ in 0.1 M KCl at varied scan rate of 10, 30, 50, 70, and 100 mV/s. The regression line of the peak current (A) and the square root of the scan rate $((mV/s)^{1/2})$ of (d) GSH-SPCE (Anodic: $y=1.6\times10^{-6}x+1.7\times10^{-6}$ $R^2=0.999$; Cathodic: $y=-1.7\times10^{-6}x-1.1\times10^{-6}$ $R^2=0.992$), and (e) bare SPCE (Anodic: $y=1.3\times10^{-6}x +2.2\times10^{-6}$ $R^2=0.981$; Cathodic: $Y=-1.2\times10^{-6}x-2.1\times10^{-6}$ $R^2=0.929$). It can be ascribed to a diffusion-dominated quasi-reversible process. The electroactive area of GSH-SPCE, calculated by the Randles-Sevcik equation, was found to be 1.34 times larger than the one of bare SPCE. (f) The EIS data (dots) and fitting (lines) of the GSH-SPCE and bare SPCE in 0.01 M $[Fe(CN)_6]^{4-/3-}$ in 0.1 M KCl. The detailed fitting results are shown in Table S3.2, in which GSH-SPCE has a larger double-layer capacitance (Cdl) and much smaller charge transfer resistance (Rct).

Table S3.2 The detailed fitting results in electrochemical impedance spectroscopy

	Chi-Sqr	Sum-Sqr	Rs(+)	Rs(Error%)	Cdl-T(+)	Cdl-T(Error%)	Rct(+)
Bare	0.00015	0.017	288.60	0.29	1.1E-06	1.79	4255.00
GSH	5.11E-05	0.0059	245.50	0.17	1.52E-05	3.15	809.90

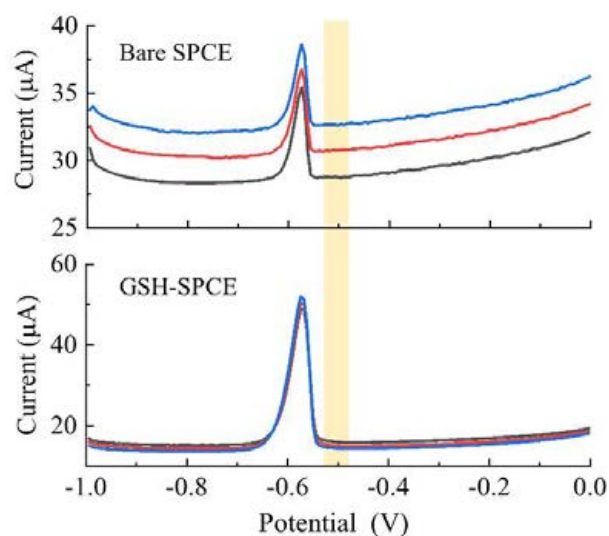|	Rct(Error%)	W-R(+)	W-R(Error%)	W-T(+)	W-T(Error%)	W-P(+)	W-P(Error%)
Bare	0.59	9458.00	12.64	12.86	19.60	0.59	2.26
GSH	2.07	10590.00	6.70	16.20	13.02	0.46	0.81

Figure S3.7 The absence of peak B in individual detection of 80 ppb Pb²⁺. The voltammograms of bare SPCE and GSH-SPCE tested in the individual 80 ppb Pb²⁺ solution. The stripping curves with different colors were obtained in three continuous measurements by the single electrode (n=3). The yellow background highlighted the absence of peak B in Figure 2(d-e) in the manuscript.

Table S3.3 The summary of the obtained sensitivity (calibration slope), Y-intercept and R^2 in all comparative experiments in this study.

HMs	Various concentrations of Cd	SPCEs	Sensitivity (μAV/ppb)	Y intercept (μAV)	R^2
Cd	Individual measurement	GSH	0.032	-0.29	0.996
		Bare	0.015	-0.19	0.990
	With 80 ppb Pb	GSH	0.0066	-0.077	0.995
		Bare	0.00053	-0.010	0.971
	With 80 ppb of Cu and Pb	GSH	0.0038	-0.12	0.928
		Bare	-	-	-
	Simultaneous measurement	GSH	0.0017	-0.024	0.991
		Bare	0.00027	-0.0018	0.841
	Various concentration of Pb	**SPCEs**	**Sensitivity (μAV/ppb)**	**Y intercept**	**R^2**
Pb	Individual measurement	GSH	0.021	-0.023	0.998
		Bare	0.0054	-0.10	0.959
	With 80 ppb Cd	GSH	0.022	-0.16	0.995
		Bare	0.0056	-0.14	0.918
	With 80 ppb Cd and Cu	GSH	0.033	0.22	0.999
		Bare	0.028	0.28	0.995
	Simultaneous Measurement	GSH	0.036	-0.27	0.994
		Bare	0.024	-0.36	0.982
	Various concentration of Cu	**SPCEs**	**Sensitivity (μAV/ppb)**	**Y intercept**	**R^2**
Cu	Individual measurement	GSH	0.021	0.15	0.984
		Bare	0.013	-0.026	0.999
	With 80 ppb of Cd	GSH	0.034	0.19	0.988
		Bare	0.033	0.10	0.994
	With 80 ppb of Pb and Cd	GSH	0.032	-0.22	0.999
		Bare	0.028	-0.16	0.999
	Simultaneous measurement	GSH	0.029	-0.10	0.997
		Bare	0.018	-0.19	0.992

Table S3.4 The LODs of GSH-SPCE and bare SPCE towards Cd, Pb and Cu in the simultaneous detection

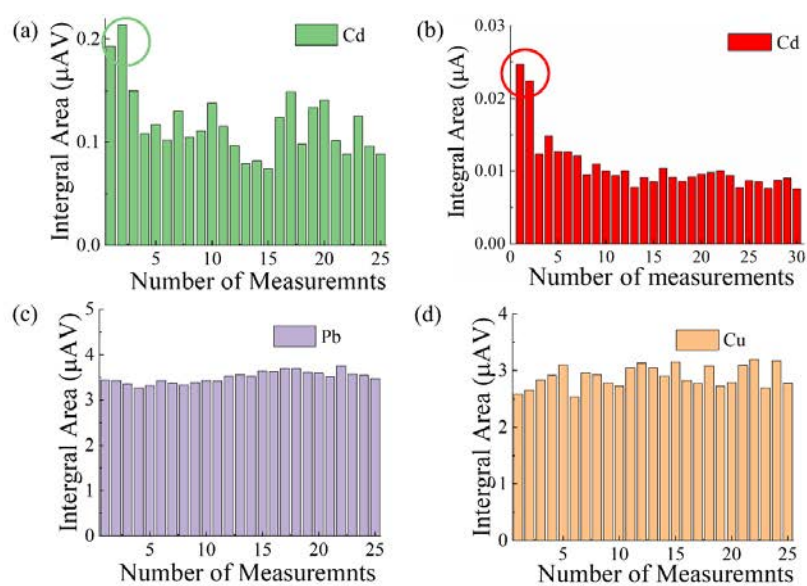|	Cd	Pb	Cu
Bare SPCE	84 ppb	18 ppb	12 ppb
GSH-SPCE	15 ppb	11 ppb	6 ppb

Figure S3.8 The data of sensing signals in repeatability study. The diagram of one GSH-SPCE in a mixed solution of 80 ppb (a) Cd^{2+}, (c) Pb^{2+}, and (d) Cu^{2+} with continuous 25 measurements for 150 min. (b) The signal diagram of bare SPCE in a mixed solution of 80 ppb Cd^{2+}, Pb^{2+}, and Cu^{2+} with continuous measurements.

Reproducibility

Table S3.5. The data of the sensitivity in reproducibility study and Student´s T-test. The sensitivities of 5 GSH-SPCEs (group GSH) and 5 bare SPCEs (group Bare), were operated by Student's T-test to investigate the static difference between group GSH and group Bare.

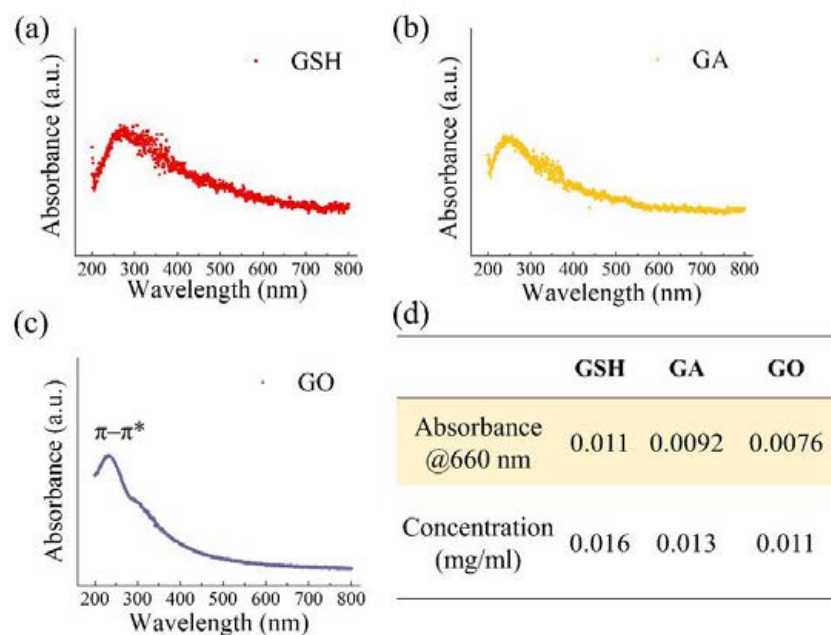| Group GSH	Group bare	Group GSH	Group bare	Group GSH	Group bare
Cd Sensitivity (µAV/ppb)		Pb Sensitivity (µAV/ppb)		Cu Sensitivity (µAV/ppb)	
0.0012	0.0003	0.032	0.029	0.045	0.046
0.0014	0.0002	0.026	0.029	0.041	0.042
0.0018	0.0003	0.035	0.028	0.046	0.044
0.0011	0.0002	0.030	0.029	0.045	0.045
0.0014	0.0002	0.029	0.030	0.046	0.046

Figure S3.9 The estimated concentration of GSH, GA, and GO was characterized by UV-Vis. The UV-Vis spectra of the obtained graphene supernatants *i.e.*, (a) GSH, (b) GA, and (c) GO after adapting the concentration with GSH by dilution. (d) The table of estimated concentrations of graphene derivatives using UV-Vis by the Beer-Lamber equation, which has been introduced in the subsection 2.3 of *Preparation of GSH-SPCE in Experimental Section*.
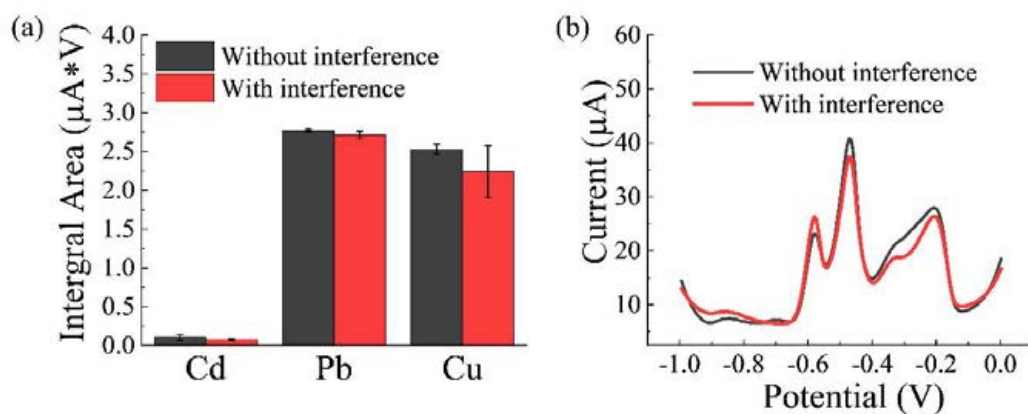
Interference from other ions

Figure S3.10 The detailed data in the interference study. The diagram of HM responses without interference (only solution of 80 ppb Cd^{2+}, 80 ppb Pb^{2+}, and 80 ppb Cu^{2+}) and with the other interferents of 400 ppb of Na^+, K^+, Ca^{2+}, Mg^{2+}, Ni^{2+}, Zn^{2+}, As^{3+}, Hg^{2+}
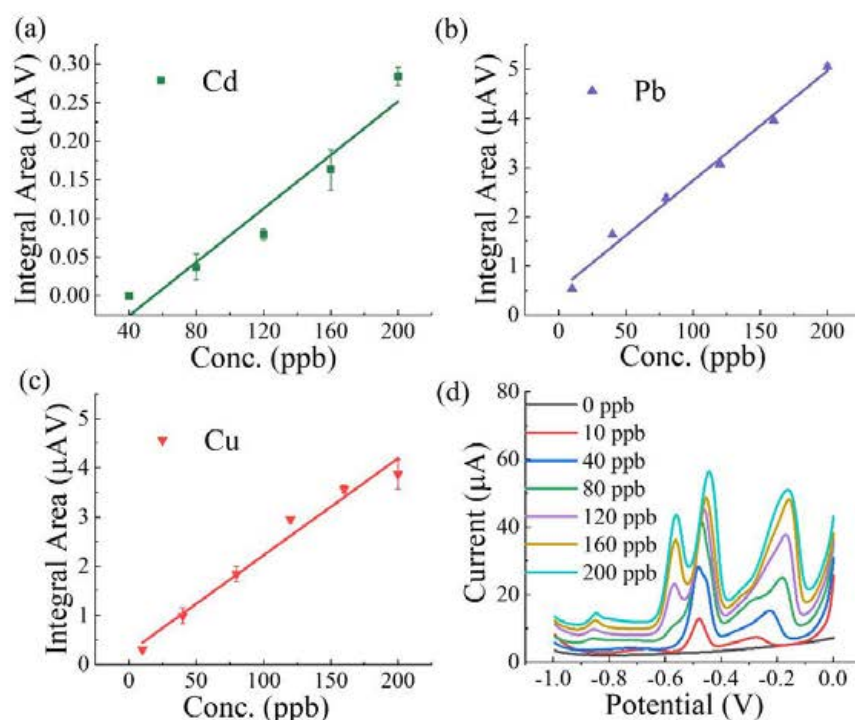
Figure S3.11 The sensing performance of GSH-SPCE in spiked tap water. The calibration of (a) Cd^{2+}, (b) Pb^{2+}, and (c) Cu^{2+} by the GSH-SPCE in spiked tap water with different concentrations of Cd^{2+}, Pb^{2+} and Cu^{2+} (1:1:1). The calibration curve of Cd, Pb, and Cu is y=0.0017x-0.095 R^2=0.936, y=0.022x+0.50 R^2=0.989, and y=0.019x+0.25 R^2=0.974 respectively. (d)The voltammograms of spiked tap water by GSH-SPCE from 0ppb to 200 ppb.

Table S3.6 The investigation of the accuracy of GSH-SPCE in spiked tap water. Recovery of mixed 90 ppb Cd^{2+}, Pb^{2+} and Cu^{2+} in simultaneous detection

	Spiked conc. HMs (ppb)	Calculated Conc.(ppb)	SD (ppb)	Recovery (%)	Conc. tested by ICP-MS (ppb)
Cd	90	73.5	5.03	81.63	92
Pb	90	73.4	1.79	81.61	94
Cu	90	72.3	4.70	80.31	94

Chapter 4

Chapter 4. All-Printed Wearable Sensor for Cu²⁺ Detection in Artificial Sweat

Wearable sensors are becoming pervasive in our society, but primarily based on physical sensors, with just a few optical and electrochemical exceptions. Sweat, amongst other body fluids, is easily and non-invasively accessible, and relatively poor of interfering species. The biomarkers of interest in sweat range from ions and small molecules to whole organisms. Heavy metals have been found to be indicators of several diseases and pathological conditions. Cu²⁺ ions in particular are correlated to Wilson's disease and liver cirrhosis among others. Nevertheless, the FSS used in Chapter 2 and Chapter 3 is not practical for wearable sensors in healthcare. Herein, we propose a fully printed microfluidic sensor for Cu²⁺ ions detection in artificial sweat with an integrated wireless smartphone-based readout— a flexible customized potentiostat. A module of reverse iontophoresis (RI) was also integrated into the miniaturized potentiostat, aiming for a controllable stimulating way of sweat perspiration. The microfluidic sensor possessed an enclosed microchannel and microchamber to manipulate the tested solution as laminar flow. The SPCE was assembled in the microfluidic sensor to detect Cu²⁺ ions by SWASV, showing a LOD of 396 ppb, a linear range up to 2500 ppb, and a sensitivity of 2.3 nA/ppb. Considering the sample volume and the sweat rate may influence the accuracy of Cu²⁺, inkjet-printed Ag nanoelectrodes were also integrated into the sensing system to detect sweat conductivity and volume. The light weightiness renders our system to be applied to the skin easily.

4.1 Introduction

Wearable sensors have been used commonly in our society and have withdrawn great attention from the scientific community. The main applications of these devices are currently healthcare and sport, with physical sensors based on gyroscopes and accelerometers and optical sensors for the measurement of the heart rate.[1] Despite performing basic operations, these wearable sensors have clearly shown the relevance of continuous wireless/remote monitoring, big data analysis, and proper results visualization.

Besides physical wearable sensors, bio- or chemical wearable sensors mainly based on electrochemical and optical platforms, have been used in the non-invasive monitoring of biomarkers including metabolites, bacteria, and hormones.[2] A very impacting application is the continuous glucose monitoring system, which measures the glucose concentration by enzymatic sensing platforms under the skin (blood or interstitial fluid) in real-time for up to 10 days.[3] Lactate measuring devices are another example using a similar approach and withdraw interest as well, mainly for sports applications.[4]

The selection of samples to be analyzed influences the design and performance of bio- and chemical wearable sensors. By definition, a wearable sensor targets non-invasive sampling; thus, the typically addressed samples are interstitial fluid, tears, and sweat. The latter is abundant and contains many biomarkers for pathologies and the general wellbeing of humans, and it possesses simple composition which indicates less interference from the sample matrix.[5] For these reasons, wearable sweat sensors have attracted relevant attention.[4,6–11]

Despite this, sweat extraction in many wearable sweat sensors is inconvenient,[12] which relies on the passive approach. This approach required the subject to keep taking physical exercise or staying in the condition at an increased temperature (*e.g.,* sauna). For this reason, using drugs or electrical currents (*i.e.,* reverse iontophoresis, RI) is emerging in wearable sweat sensors as an active approach.[5] However, in both cases, the amount of excreted sweat during a unit of time (*i.e.,* the sweat rate) would vary during sampling, which affects the concentration of the targets in sweat.[4] It poses the risk of inaccuracy in the analysis, and thus, normalization of the obtained concentration by sweat rate has been utilized to improve precision and accuracy.[13–16] Hence, an integrated sweat volume/rate sensor is demanded in a wearable sweat sensor. Besides being applied in the normalization, sweat rate itself offers valuable information about health condition and thus has been measured by microfluidic wearable devices.[17,18]

In addition to these issues, sweat wearable sensors are mainly disposal devices with a short duration, and the concept of continuous monitoring has rarely been met.[19–22] In the few studies presenting continuous detection, the wearable sweat sensors only measured simple characteristics of sweat *e.g.,* pH or alkali metal ions.[18,23]

Apart from the mentioned characteristics, sweat conductivity is also a well-known target for the diagnosis of cystic fibrosis (CF), serving as a substitute for the standard quantification of the Na^+ and/or Cl^- ions. CF is an inherited disorder, causing a failure of the innate airway defense mechanism and damage to the digestive system and other organs. CF is frequently accompanied by a high concentration of salts in sweat; the associated cut-off sweat conductivity is over 90 mM for the CF diagnosis.[24] Herein, sweat conductivity is expressed as the conductivity measured by the same sensor in sodium chloride (NaCl) solution at the specified concentration, and the value of the specified concentration is defined as sweat conductivity, with the unit of mM.

Additionally, the HMIs present in sweat are interesting analytes, as they could reflect an extensive intake of the HMIs (such as Cu^{2+}, Zn^{2+}, Cd^{2+} and Pb^{2+}) that discharge through sweat.[25] Some reports claim that these ions would discharge more through sweat rather than urine or blood.[26–28] Amongst them, Cu^{2+} ions, for example, are involved in many pathological processes.[29] For instance, the imbalance of Cu^{2+}/Zn^{2+} ratio is suspected to be correlated to coronary heart disease.[30] The abnormal concentration of Cu^{2+} ions is also correlated with rheumatoid arthritis, [31] Wilson's disease, [32] and liver cirrhosis.[33,34] Furthermore, Cu^{2+} ions in sweat are also related to physical exercise and heat stress.[35–37]

However, few biosensors have targeted Cu^{2+} and other HMIs in sweat as the format of wearable sensors. In 2010, Souza et al. initiated to report the detection of Cu^{2+} in sweat with a gold microprobe (fabricated by photolithography) using SWASV. However, the presented system was not truly wearable, due to the applied standard three-electrode electrochemical setup.[38] In 2021, Bagheri et al. proposed an electrochemical sensor based on gold nanoparticles-decorated paper for the sensitive detection of Cu^{2+} in human sweat and serum. The applied materials were biocompatible and sustainable: a SPCE was printed on cellulose-based paper on which wax was printed to create a hydrophilic fluidic channel. This device was proved to be very effective for Cu^{2+} determination for single use with the LOD of 3 ppb, linear range up to 400 ppb and recovery between 93% and 101% in the spiked sweat. Despite these very promising characteristics, this system is not fully integrated yet, and needs a miniaturized potentiostat to perform wearable quantification.[39] Additionally, in the case of abundant sweating caused by emotion and/or temperature, a high and pathological amount of Cu^{2+} could be diluted in the high volume of sweat with underestimated results. The presented HMIs sweat sensor ignored the normalization of the detected value with respect to the sweat rate during the measurement.

In this work, we proposed an all-printed microfluidic sweat sensing system which is primarily composed of: a) a laser-patterned bi-adhesive tape as the hollow part, b) inkjet-printed electrodes (as the base of the fluidic channel) for the measurement of the sweat volume/rate and RI, c) a SPCE (as the cover of the fluidic channel) for electrochemical determination of Cu^{2+}, and d) a flexible customized and miniaturized readout device including a potentiostat

operating SWASV, a module operating RI and a wireless communication module (Bluetooth) for transmitting data to a smartphone. The structure of (a)-(c) is shown in Figure 4.1.The whole system was flexible, lightweight, managed remotely, and applied directly on the skin with a patterned bi-adhesive tape (Layer 1, Figure 4.1). As far as we know, this is the first fully integrated system to detect Cu^{2+} in sweat with compensating sensors (*i.e.*, sweat conductivity and volume nanosensors), and a miniaturized flexible potensiostat as the wearable format. It may allow for the normalization of Cu^{2+} concentrations in sweat on the base of the sweat rate, and the flexible potentiostat could facilitate its practical use.
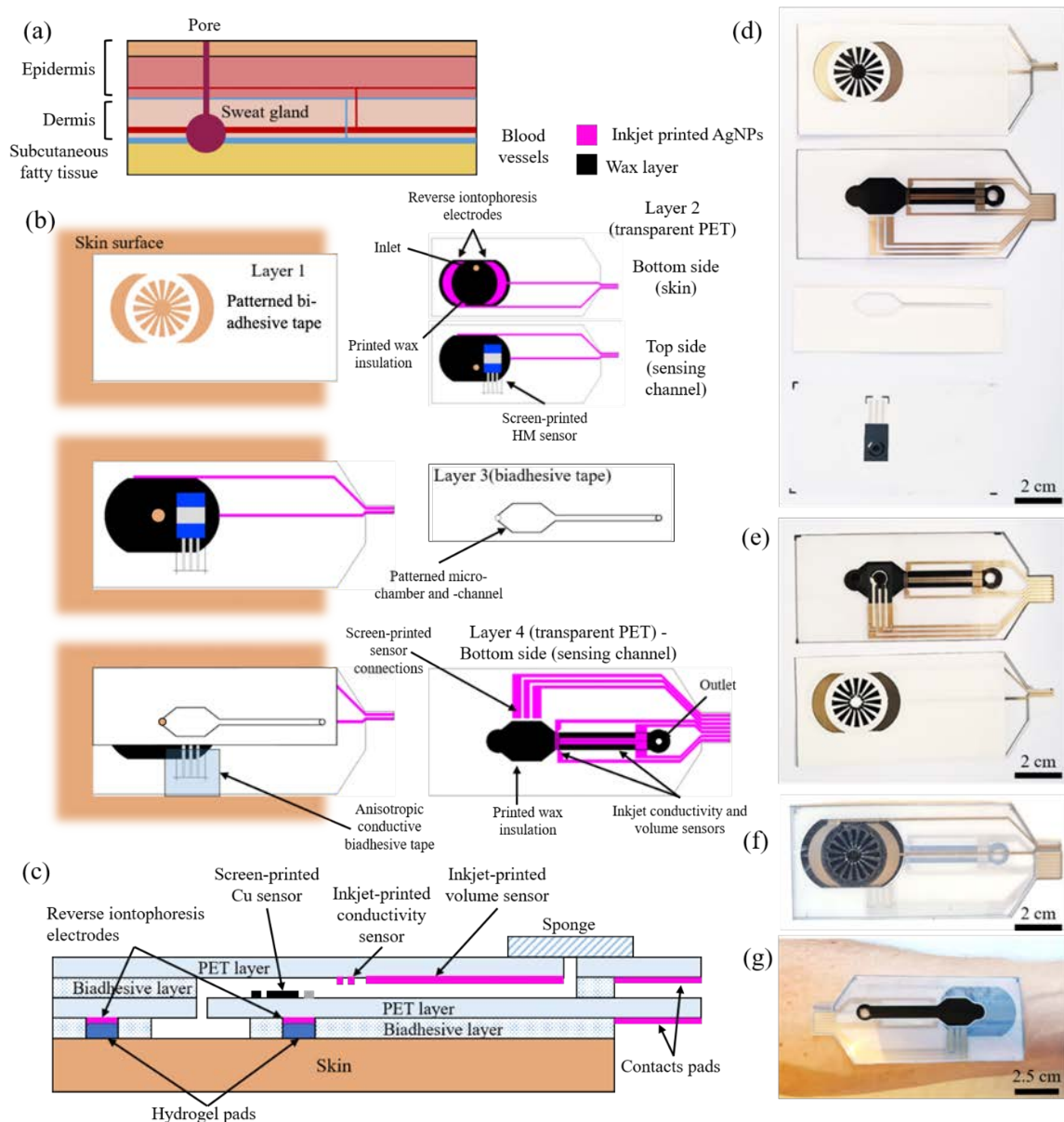

Figure 4.1 (a) Scheme of the skin tissue vertical structure, (b) diagram illustrating the structure of the assembled device and of its layers: layer 1 – patterned bi-adhesive tape (by laser cutting) for skin adhesion and sweat collection; layer 2 – inkjet-printed electrophoresis electrodes and connections (bottom), and SPCE for the Cu detection (top); layer 3 – patterned bi-adhesive tape for the microchannel and microchamber and anisotropically conductive tape (blue

square) for the electrical connection of the SPCE contacts with the layer 4 inkjet lines; layer 4 – inkjet-printed electrodes for the conductivity and volume measurements. (c) Cross-section of the assembled device on the skin. Wax was used to avoid infiltrations in the porous PET used for high-quality and sinter-free inkjet printing of the AgNPs layout (not indicated in the cross-section for simplicity). On the right, (d) pictures of the system are divided into its parts, (e) partially assembled, (f) fully assembled, and (g) applied on the forearm skin.

4.2 Experimental Section

4.2.1 Reagents and Apparatus

37% Hydrochloric acid (3203312.5 L), standard heavy metal solutions (Cu^{2+}, Zn^{2+}, Pb^{2+}, Ni^{2+}, 1000 ppm, AAS grade) were purchased from Sigma Aldrich. The potentiostat used for the Cu^{2+} calibration was a Palmsens EmStatBlue with the PStrace 5.8 software. A Metrohm Autolab PGSTAT12 with a FRA2 module and NOVA software was used for the impedance-based characterizations of the conductivity and the volume inkjet-printed sensors. The artificial sweat used for the system validation was composed of 0.1 M NaCl, 0.1 wt% KCl, 0.1 wt% lactic acid, 0.1 wt% urea in acetate buffer (0.1 M, pH=4.5) as reported elsewhere.[40]

4.2.2 Device Setup

The device was composed of four layers shown in Figure 4.1b. Layer 1 was fabricated by a piece of bi-adhesive tape with a specific excavated part by a laser printer (Rayjet 50™ CO_2 laser) for collecting the excreted sweat by RI electrodes. Layer 2 was made of a porous PET substrate (from Mitsubishi Paper Mills limited™), with inkjet-printed RI electrodes on the bottom side, and SPCE for the detection of the Cu^{2+} ions on the top side. Layer 3 was made of bi-adhesive tape, with an evacuated pattern of a fluidic chamber and channel in series but leaving the contacts of SPCE uncovered. Then, a patch of conductive anisotropic bi-adhesive tape, in which conducting electricity only goes through the vertical direction and insulates along the horizontal direction, covered the SPCE contacts. On Layer 4 (the last layer), conductivity and volume nanosensors, and necessary conductive contacts (magenta color in Figure 4.1b) were inkjet-printed on another porous PET substrate, to enclose the fluidic chamber and channel. The inkjet-printed contacts were aligned with the ones of SPCE on the second layer. At the end of the micro-channel, a hole was punched through Layer 4, allowing the sample to exit and contact with a paper-based sponge for sample evaporation.

The two conductive contacts associated with RI on Layer 2 and the seven conductive contacts of all the sensors on Layer 4 were aligned as a 14 mm-width pad to fit within the connector of the readout device.

4.2.3 Inkjet Printing and Passivation

All the conductive contacts, conductivity and volume nanosensors were printed with AgNPs, (from Mitsubishi Paper Mills Silver Nano™ AgNP ink (NBSIJ-MU01)) on the porous PET substrate from Mitsubishi Paper Mills (NB-TP-3GU100) by an EPSON XP15000 office printer, in which the AgNP ink had been loaded in an empty cartridge (magenta) to replace the original one. The porous PET substrate has a porous coating on a PET substrate, which drains the ink for instant drying, and the released chemical regents from the porous pad sinter nanoparticles chemically. The working principle is introduced in the subsection of inkjet printing in Chapter 1.2.

For sensing the conductivity and volume of sweat in the micro-channel, two sets of electrodes were printed. The first set was finger-like parallel electrodes with a width and gap of 400 μm which were perpendicular with respect to the orientation of the microchannel and crossed the microchannel completely with a length of 2 mm. The second set of parallel electrodes with a gap of 200 μm was alongside the microchannel of 30 mm in length.

Afterward, inkjet-printed devices were kept for 72 h at room temperature in a closed Petri dish in dark condition.[41] Then, a layer of wax (black color, Xerox Phaser 8850) was printed in the area over and around these nanosensors. After wax printing, the devices were kept at 95℃ for 20s to partially melt the wax. To achieve better penetration, the heating procedure was repeated once for 5 min. Excessive wax on the surfaces of nanosensors was removed and adsorbed by papers *via* passing the printed devices in a laminator embedded with two normal office papers.[41]

4.2.4 Patterning Bi-adhesive Tape and Assembling Microfluidic Devices

A sheet of Oriented Polypropylene (OPP) bi-adhesive tape in A4 size (Tosingraf, Italy) was patterned by a laser printer in the cutting mode (Rayjet 50™ CO_2 laser; power: 6.9%, number of passages: 4, speed: 100%) to excavate a microfluidic channel (Layer 3 in Figure 4.1) and desired pattern on Layer 1 for sample collection. Similarly, a piece of 3M anisotropic conductive film (ACF, conducting only through its thickness) was cut to cover the SPCE's conductive paths. It connected the SPCE's contacts to inkjet-printed connectors on the porous PET substrate.

Before assembly, the inkjet-printed layers and exposed wax surface were shortly treated (15s) by atmospheric plasma to increase the hydrophilicity. Then, the devices were assembled as shown in Figure 4.1b-d, with the inkjet-printed devices enclosing the microchannel as a cover. As the last step, the whole microfluidic device was passed through in a laminator (Lamigator IQ, Renz, Germany) between two sheets of office paper to homogeneously compress it to avoid leakages.

4.2.5 SPCE Fabrication

The SPCEs were fabricated using a DEK248 printer machine (DEK, Weymouth, UK) with the same protocol as introduced in Chapters 2 and 3. The substrate was cleaned with deionized water and ethanol, then dried with nitrogen and pre-heated at 110°C for 30 min to evaporate solvents and prevent deformations in the following steps. The printing sequence on the prepared PET substrate and the used inks are the following: (1) Ag paste (C2180423D2 SILVER PASTE-349288, Sun Chemical) for conductive connections, (2) Ag/AgCl paste (Loctite EDAG AV458, Henkel) for the reference electrode, (3) carbon paste (C2030519P4 CARBON SENSOR PASTE-267508, Sun Chemical) for the working and counter electrodes, (4) and the insulating layer (D2070423P5 DIELECT PASTE GREY, Sun chemical). Heating at 110°C for 30 min was necessary to cure the inks in the oven after every printing step. The SPCE was placed on top of Layer 2 as the base of the microfluidic channel and chamber.

4.2.6 Electrochemical Cu^{2+} Detection by SWASV and EIS

To avoid the bubbles before measurements, the microfluidic device was firstly rinsed with artificial sweat which was then purged away by a N_2 gas flow. Then, the microchannel and chamber were filled again with artificial sweat that was staying for 10 min. Afterward, the microfluidic device was emptied by the N_2 gas flow.

Artificial sweat containing Cu^{2+} was filled in the microfluidic device and was measured by SWASV, whose working principle has been introduced in Chapters 2 and 3: first, the target ions are reduced on the working electrode surface, and then, the reduced metals are re-oxidized to ions, showing varied potential and current as a voltammogram.

During the deposition step, a constant negative potential of -0.66 V was applied to the WE for 200s. During the stripping step, the potential was swept from -0.66 V to 0 V in a square-wave pulse with a frequency of 25 Hz, an amplitude of 30 mV, and a potential step of 6 mV. Between these two steps, an equilibrium time (20s) was applied, in which the flow should stop, and the potential kept the same value as the deposition potential (-0.66 V).

For the EIS measurement by the inkjet-printed nanosensors, the device was connected to a Metrohm AutoLab PGSTAT12 (FRA2) potentiostat, and operated the EIS in triplicate at 100 kHz, with 10 mV AC and 0 V DC.

4.3 Results and Discussion

4.3.1 Design of Printed Microfluidic Device

The printed microfluidic device was designed and fabricated with three integrated sensors: a SPCE for Cu^{2+} detection, a conductivity nanosensor (perpendicular with respect to the microchannel) and a volume nanosensor parallel to the microfluidic channel (Figure 4.1c). The SPCE operate SWASV for the Cu^{2+} ions detection; the conductivity and volume nanosensor

were composed of conductive AgNPs, and utilized their measured impedance as a function of sweat conductivity and volume on the basis of Ohm's law due to the applied high frequency.

During the measurement, the sampled sweat filled first in the SPCE chamber (HM micro-chamber), then passing through the conductivity nanosensor, and finally initiated to cover the volume nanosensor in the micro-channel (Figure 4.1c) with a dead volume of ~27 µl. When the HM chamber was filled, the conductivity nanosensor can trigger a signal for the user to start the Cu^{2+} measurement. Since the volume nanosensor was able to measure the volume of collected sweat in a specific period, the concentration of Cu^{2+} ions could be normalized by the sweat rate.

4.3.2 Characterization of Microchannel and HM Microchamber

Microchannel and HM microchamber were firstly investigated to verify if the hollow structure was successfully created. The cross-section along the microchannel (Figure 4.2a) was obtained by immersing the microfluidic device in liquid nitrogen, followed by using a razor blade and hammer to achieve a net cut and preserve the device structure. The cross-section of the volume sensor clearly showed that the microchannel was surrounded by Layer 2 (the substrate of SPCE) on top and the inkjet-printed device at the bottom, with the bi-adhesive tape blocking the lateral side. The microchannel was less than 100 µm in thickness, in accordance with the results of 3D profilometry (~99 µm, Figure 4.2a inset), which offers the capillary force. Additional profilometry measurement showed that the thickness of the inkjet-printed volume nanosensor was approximately 600 nm, with the gap width of 150 µm approximately.

The HM microchamber was characterized by the same method. In Figure 4.2b, a stacked structure composed of porous PET substrate (with printed wax), the microchamber, the SPCE, and its PET substrate is depicted. The height of the microchamber was the same as the one of the microchannel (˜99 µm), which means that the bulged SPCE (compared with the bare PET substrate) did not create any relevant deformation on the microchamber. The morphology of the carbon paste electrode was also investigated (Figure 4.2c) showing the expected carbon flakes and particle structures.[42] The carbon layer is estimated to have a thickness of 35 µm approximately.
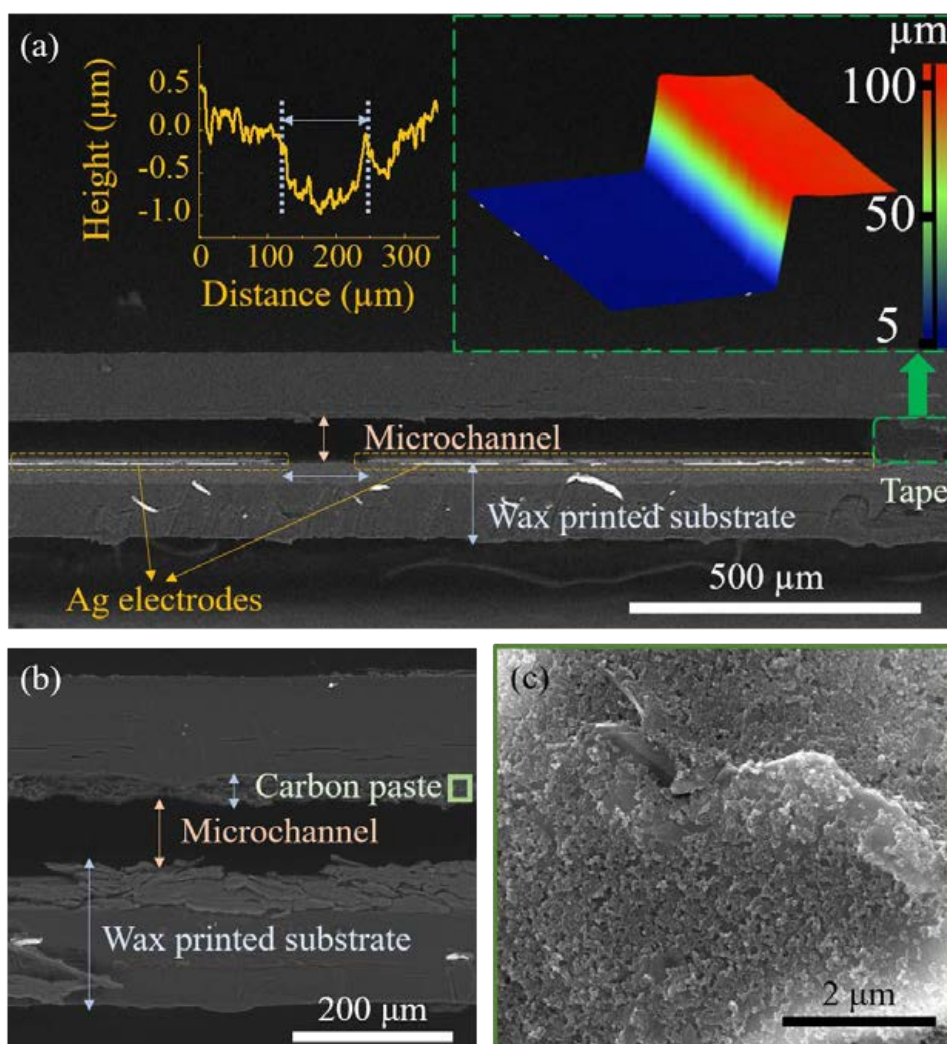
Figure 4.2 Cross-section of the microchannel, profilometry of the gap between two printed Ag electrodes (Inset left) and 3D profilometry of the open microchannel border (Inset right) (a), the cross-section of the copper detection chamber (b), and SEM picture of the SPCE working electrode (c).

4.3.3 Sensing Performance of the Conductivity and Volume Nanosensors

The frequency for the impedance measurement by conductivity and volume nanosensors was firstly optimized as 10 kHz to achieve a resistive response (instead of a capacitive response), which demonstrates the closest phase value to zero in 95 mM NaCl solution with measurable signal without noise compared to other frequencies.

The microfluidic device was then tested to define the sensing performance of the conductivity nanosensor with a variety of NaCl solutions at different concentrations ranging from 5 to 156mM, which were corresponding to the conductivity from 0.60 to 17.03 mS/cm (on the basis of the linear relationship presented elsewhere [43].

The impedance of the conductivity nanosensor dropped from 100 kΩ (empty channel) to 30 kΩ when a NaCl solution (5 mM) reached the electrodes, showing its capacity as an electrical trigger. Further, the staircase calibration of the conductivity nanosensor was operated and the results are shown in Figure 4.3a. The impedance decreased as the NaCl concentration increased. Figure 4.3a has been marked with different colors associated with the CF disease cut-off sweat salts concentrations: green for the healthy condition, orange for the dangerous concentration requiring further investigation, and red for pathologic condition (NaCl concentration over 90 mM).[24] The measured admittance (*i.e.*, the reciprocal of impedance) was perfectly proportional to the NaCl concentration (Admittance $=2.95\times10^{-6}$ [NaCl]$+1.17\times10^{-5}$, $R^2=0.99$) as shown in Figure 4.3b.
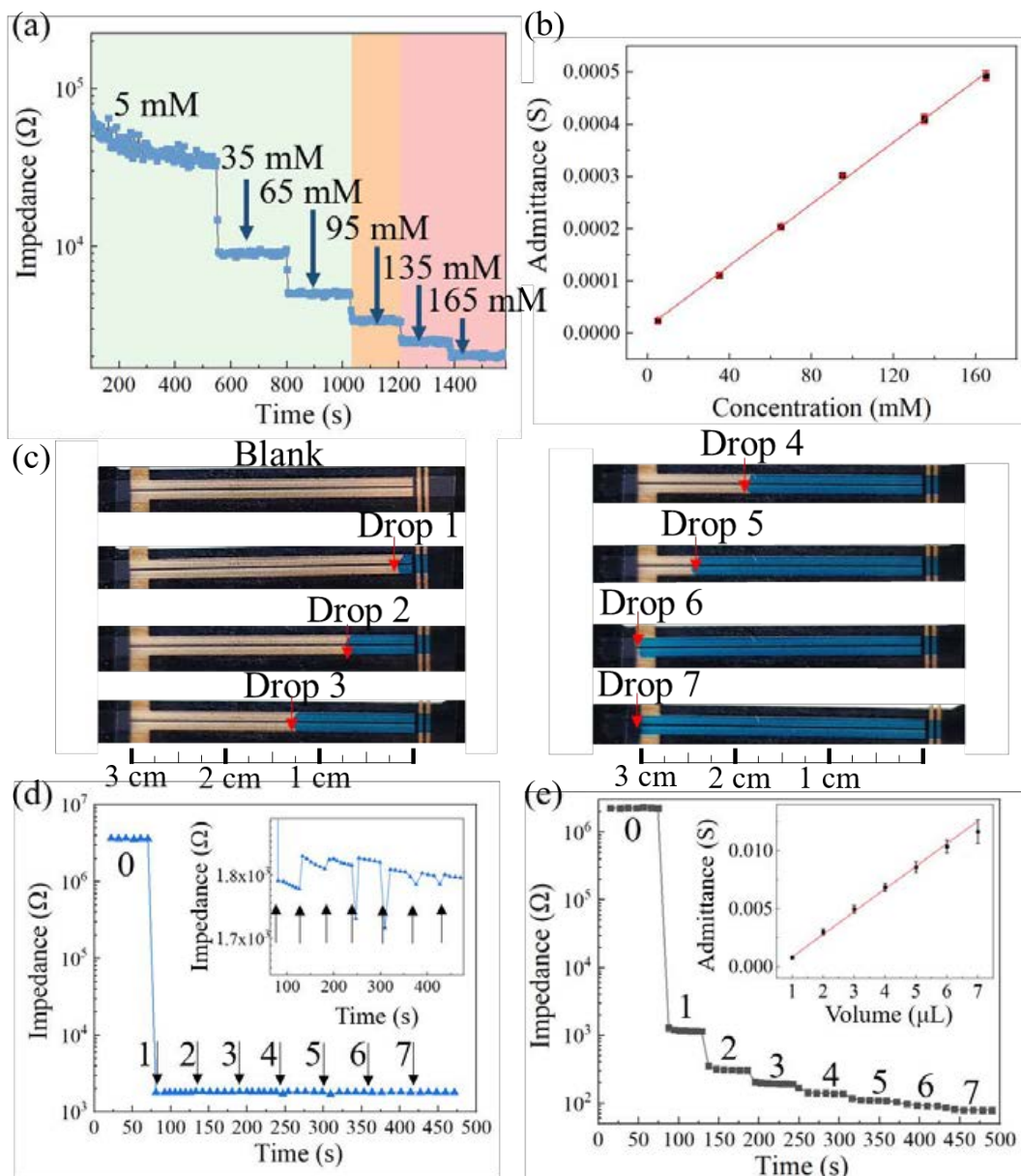

Figure 4.3 (a) Staircase calibration of the conductivity nanosensor impedance with NaCl at a frequency of 10 kHz. CF diagnosis relevant ranges marked with colors (green=healthy, orange=suspicious, red=pathological), (b) the admittance calibration curve, (c) digital photos

of the microchannel in correspondence to 1 µl colored aqueous drops at the nanosensor inlet, (d) the impedance of the conductivity nanosensor and (e) the volume nanosensor at 10 kHz in correspondence to artificial sweat introduced drop by drop, and (inset) the calibration of the volume nanosensor by means of its admittance.

To examine the performance of the volume nanosensor, different volumes of artificial sweat were introduced into the printed microfluidic device, which can be intuitively seen in Figure 4.3c. Meantime, the impedance of the conductivity nanosensor was recorded too, with a minimal change with the varied volume, showing its resilience to the different amounts of the tested solution (Figure 4.3d).

Interestingly, by the capillary force, the solution can be driven to move forward as a quasi-rectangle shape, which may be attributed to the tested flow is a laminar flow (in Figure 4.3c). Thus, the admittance of the volume nanosensor can be simplified as conductance at the such high frequency of 10 kHz and almost conform to the ideal Ohm's law.

Theoretically, the conductance should be proportional to the lateral-side area of the conductive solid, in our case *i.e.*, microchannel thickness (a constant) × liquid length, for the volume nanosensor resides alongside the microchannel. The experimental results were verified in Figure 4.3e (inset, Admittance=0.00169×Volume R^2=0.99) that the admittance of the volume nanosensor has a linear relationship with the injected volume. In this way, the calibration in the artificial sweat between the obtained admittance of the volume nanosensor (A_{volume}, S) and the volume (µL) was constructed due to the high R^2.

$$A_{volume} = 0.00169×Volume \qquad\qquad (Eq.\ 4.1)$$

Despite this, it is necessary but inconvenient to construct the calibration between the volume and admittance in every unknown solution. A normalization method could serve for different solutions (normalization of admittance), which was achieved by mathematical calculation based on the obtained results:

According to Ohm's law, the conductance is only determined by the conductivity of the tested solution and the geometry of the tested solution between two electrodes; the conductance is proportionate with conductivity. Hence, the conductivity of the tested solution has been involved in the conductance (or admittance at the high frequency in our case) of the conductivity nanosensor, for it has a fixed geometry of two-finger electrode across the microchannel. Accordingly, the conductance of the conductivity nanosensor can be applied in constructing the linear relationship between the conductance of the volume nanosensor and the collected volume shown in Eq. 4.2.

$$A_{volume} = k·A_{conductivity}·Volume \qquad\qquad (Eq.\ 4.2)$$

The volume nanosensor's admittance (A_{volume}, S) is proportional to the volume by a constant (k, μl^{-1}) and the conductivity nanosensor's admittance ($A_{conductivity}$, S) (Eq. 4.2).

As such, in our study of using artificial sweat, $k \cdot A_{conductivity}$ is equivalent to 0.00169 S μL^{-1}, and $A_{conductivity}$ had been obtained in Figure 4.3d (~1800 Ω). Therefore, a constant k can be calculated which is equal to 3.042 μl^{-1}. Therefore, the volume of sweat can be calculated from the admittance measured by the two nanosensors as:

$$Volume = A_{volume} / (3.042 \times A_{conductivity}) \qquad (Eq.\ 4.3)$$

The eq. 4.3 can be applicable in detection the solution with similar to the artificial sweat in our study to obtained better accuracy with convenience.

Besides, the estimation of the filling time of the microfluidic device is discussed. The sweat rate commonly ranges from 0.02 to 20 nL/min/gland.[44] In a sedentary state at room temperature, the sweat rate is quite low (0.02-0.3 nL/min/gland), hence, sweat induction methods (*e.g.*, applying thermal stress, iontophoretic delivery of nerve stimulants, reverse iontophoresis, and physical activities) are generally used.[45]

As an example, the average sweat rate of an adult after 30 min walking, without any stimulation at room temperature is 15 nL/min/gland,[46,47] and the gland density is from 51 to 111 glands/cm²,[48] hence, the average sweat rate ranges from 0.765 to 1.665 $\mu L/min/cm^2$. Considering that the collection area of our device is 1.8 cm², the sweat volume is estimated from 1.38 to 3.00 μL per minute. Therefore, in this specific case and without any stimulation, the filling time for the SPCE chamber would be between 16 and 19 min, considering that the dead volume is 27 μL. After the filling of the HM microchamber, the microchannel could be filled up within 10 min.

Therefore, the active stimulation of sweat, *e.g.,* by reverse iontophoresis is favorable and expected to increase significatively the efficiency of sweat secretion. For this reason, the active RI module was integrated into a flexible mini-potentiostat which will be introduced in the last section.

4.3.4 Sensing Performance of SPCEs in the Microfluidic Device

The SPCE in the printed microfluidic device was characterized with the $[Fe(CN)_6]^{4-} / [Fe(CN)_6]^{3-}$ redox probe, and then tested in artificial sweat to detect Cu^{2+} ions with varied concentrations using a commercial potentiostat.

Figure 4.4a shows the CV operated in 5 mM $[Fe(CN)_6]^{4-} / [Fe(CN)_6]^{3-}$ in 0.1 M KCl solution. Well-defined and quasi-reversible redox peaks were observed: the ratio between the anodic peak current (5.66 μA) and the cathodic one (-5.47 μA) is almost the same. The oxidative and

reductive peak potential is 0.28 V and -0.01 V, respectively, with a ΔE of 0.29 V, matching the results of other SPCEs reported elsewhere.[49]

Artificial sweat spiked with different concentrations of Cu^{2+} ions in the range between 500-2500 ppb was tested by the printed microfluidic device. The testing range was selected referring to a previous study reporting a healthy range of 240-2400 ppb.[50]
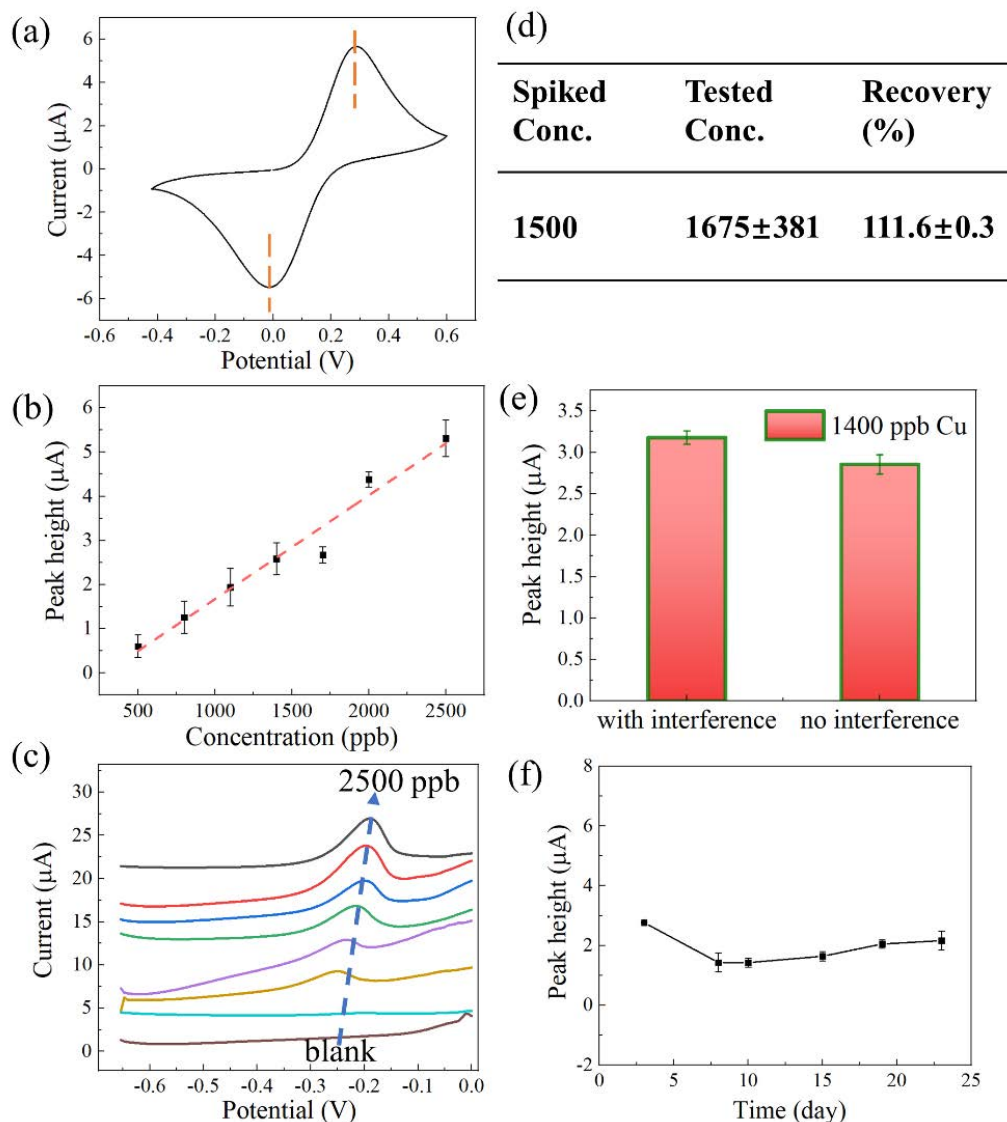

Figure 4.4. (a) CV measurement of 5 mM $[Fe(CN)_6]^{4-}$/ $[Fe(CN)_6]^{3-}$ in 0.1 M KCl solution by the SPCE in the microchamber, (b) the calibration of Cu^{2+} in artificial sweat by the SPCE in the microchamber, (c) voltammograms from 0 to 2500 ppb Cu in artificial sweat by SPCE in the microchamber, (the plots were stacked for better visualization of the variation of the peak height with respect to each baseline.) (d) recovery test with 1500 ppb Cu, (e) the comparison of the peak currents with and without interference from other ions, and (f) the peak currents detecting 500 ppb Cu^{2+} ions by the sensors fabricated in the same batch over time.

The current peak height of Cu^{2+} showed a good correlation with the varied concentrations ($I_p=0.0023\times[Cu^{2+}]-0.67$, $R^2=0.95$) as shown in Figure 4.4b. The estimated LOD and LOQ were 396 ppb and 1322 ppb, respectively. The LOD and LOQ were calculated as 3 and 10 times the standard deviation of the intercept over the slope of the calibration curve respectively, as reported in the International Conference on Harmonization's (ICH) Q2 Validation of Analytical Procedures.[51]

The corresponding voltammograms in Figure 4.4c showed a potential shift to positive potentials with increasing concentrations. This effect could be ascribed to the different deposition sites or surface morphology during the deposition of different amounts of Cu^{2+} ions.[52,53]

Once the calibration was completed, a recovery test was performed to test accuracy. Artificial sweat spiked with 1500 ppb Cu^{2+} was tested to achieve the corresponding peak current value, which was then substituted into the calibration equation. The calculated concentration is ~1675 ppb, with a recovery of 111.6% (Figure 4.4d). An interference test was performed to investigate the device selectivity with the existence of other cations typically present in sweat (*i.e.*, 120 ppb Mg^{2+}, 300 ppb Ni^{2+}, 0.5 ppb Cd^{2+}, 1300 ppb Zn^{2+}, 8000 ppb Ca^{2+}, 1600 ppb Fe^{3+}).[39] With interference, the signal of 1400 ppb Cu^{2+} was approximately 3.17 µA; compared to the condition without interference (2.85 µA), the result proved the interference from other cations in sweat can be considered negligible in our system (<10%, Figure 4.4e). The pH dependence of the microfluidic device was studied as well (pH=4, 4.5, 6), with reference to the pH range of healthy people,[54] showing that the quantification of Cu^{2+} was partially affected by pH variations in this range with RSD=22%. Besides, our sensing system is for *in-situ* sweat detection and the typical acidification for sample treatment is not practicable anymore; considering the possibility of pathological situations that may induce severe pH changes, the final Cu^{2+} detection signal may be further influenced. Additional pH sensors can be integrated into the presented sensing system to compensate for the effect in the future.

The shelf life and reproducibility of our system were investigated by fabricating a batch of devices on Day 1. Artificial sweat containing 500 ppb Cu^{2+} ions was used to test the printed microfluidic devices every 2-4 days for a total duration of 23 days. The peak height fluctuated around 1.91 µA with RSD= 27% (Figure 4.4f). However, after 23 days, due to the loss of hydrophilicity from the plasma treatment over time, the testing solution was impossible to enter the microfluidic device.

4.3.5 Wearable Potentiostat

A wearable potentiostat device instead of bulky benchtop equipment is more practical to be worn on the human body. Hence, aiming for a smaller size, less weight and flexibility, we designed and fabricated a potentiostat on a flexible PCB board integrating all the components required for electrochemical measurements and a wireless data transmission module to

communicate with a mobile phone. The system was built on a commercial electrochemical chip (LMP91000 chip), in which an integrated potentiostat is able to perform both two- and three-electrodes electrochemical measurements. The chip in our system was controlled by a programmable microcontroller, which in turn connected to a low-power Bluetooth module for wireless communication. To achieve a user-friendly interface, a customized application based on the Android system was developed, in which electrochemical measurements such as amperometry, CV, and square wave voltammetry can be operated with the parameters set by users. Furthermore, the system was designed to integrate a reverse iontophoresis module for active sweat sampling as proved in previous publications, allowing for stimulating the perspiration when needed. [55–57] The whole platform also has a very low power consumption, which is supplied by a common 3V button battery.

A basic investigation of the flexible potentiostat was performed using artificial sweat containing Cu^{2+} ions. It was controlled by the smartphone wirelessly *via* Bluetooth. The set parameters were almost the same as the ones used in previous sections (*i.e.*, deposition time 200s, equilibrium time 20s, deposition potential −0.66 V, square-wave pulses with the frequency of 25 Hz. However, due to the limited potential resolution of the chip, both the amplitude and potential step of square waves were adjusted to 60 mV.

Besides, the sampling time of the flexible potentiostat influenced the sensing signal of Cu^{2+} ions. Initially, 10 ms was employed to sample the current, allowing for four sampling data in one period. As the first several measurements involved the peak current in the result, and thus induced inaccuracy where the Cu^{2+} stripping peak was unobservable. Therefore, more sampling spots with shorter interval was attempted with the sampling time of 3 ms—the best resolution that the chip is able to achieve. The optimization of sampling time renders the Cu^{2+} stripping peak to be identified.

With these optimized parameters, the flexible potentiostat (in Figure 4.7a) was performed in the artificial sweat spiked with different concentrations of Cu^{2+} ions. First, the spiked solution (~100 μL) was directly pipetted on the SPCE, by which SWASV was operated. The obtained voltammograms (in Figure 4.7b) show an increasing peak at higher Cu^{2+} concentration. Based on their peak intensity at various concentration, a linear calibration was defined (inset, I_p=0.081×[Cu^{2+}] + 23.78, R^2=0.98). As a comparison, the spiked solution (~27 μL) was filled into the microfluidic device, by which the detection of Cu^{2+} (500 ppb, 1400 ppb, and 2500 ppb) was operated with the obtained results shown in Figure 4.7c,d. Due to the spatial limitation of the microfluidic device, the peak intensity of Cu^{2+} is much lower than the one by the dropping method. Despite this, the printed microfluidic device was still able to distinguish the difference between low, medium, and high concentration levels (Figure 4.7d).
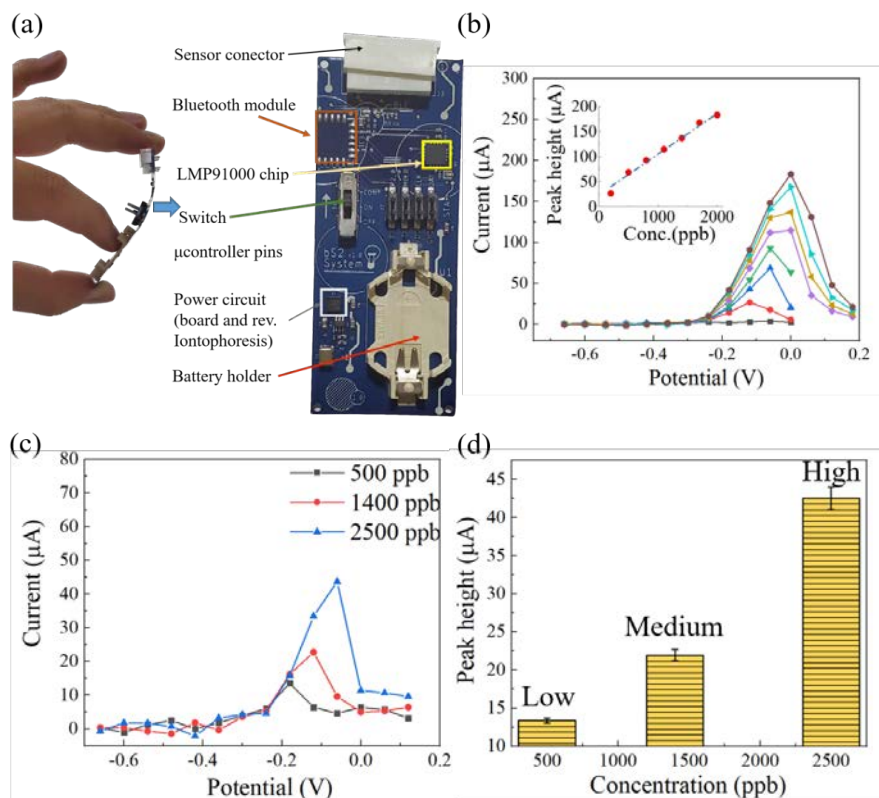
Figure 4.7 (a) Picture of the flexible PCB board including a miniaturized potentiostat module and scheme of the device (b) the measurement by the flexible PCB board to communicate with a mobile phone with directly dropping artificial sweat on the SPCE, (c) the voltammograms of the printed microfluidic device read by the flexible PCB board and transmit to the mobile phone, and (d) the diagram of the corresponding peak height.

Finally, besides the flexible potentiostat being bendable, the doubt was aroused whether the printed sensors can bear bending effect without the influence on the conductivity, to conform the curvature of natural skin (Figure 4.8a). In particular to the inkjet-printed paths with thin thickness, they are risky to detach from the surface of substrates compared to the SPCE. We therefore measured the resistance variation of inkjet-printed lines in a cycle of being flat, bent, and recovered. Only minimal variations of resistance were found in Figure 4.8b-d. Furthermore, we checked the resilience of the microchannel structure by bending the device 10 times on a cylindrical surface (shown in Figure 4.8c) and adding a blue coloring to the device inlet after repetitive bending. During the test, anything suspected to disturb the tested flow was not observed.

Despite all these results, since our sensing system is driven by capillary force, severe bending should be avoided from damage during operations. However, we would like to remark that the positioning of our system should be performed in anatomical locus favoring the natural movements of the subject and maximizing the comfort of use. Therefore, some parts of the human body could be more suitable than other parts, such as the side of the back, the proximal/distal parts of the arm (Figure 4.8a), and the lower back. All these loci are relatively flat and naturally do not involve severe bending.

Figure 4.8 (a) The microfluidic device was applied to the distal arm skin. (b) The resistance of connecting the AgNP line without bending. (c) The resistance of connecting AgNP line bent on a cylinder with a diameter of 95 mm. (d) The resistance measurement of the connecting path on the flat substrate after bending.

4.3.6 Comparison with Other Studies

To further explore the importance and novelty of this work, other recent sweat sensors for HMIs detection have been listed in Table 4.1.

Table 4.1. Comparison with other heavy metal and conductivity sensors for sweat analysis

Targets	LOD (ppb)	Sensitivity	Calibration range	Electrode	Fabrication techniques	Sweat volume	REF
Na^+	-	56 (mV/decade)	15-120 mM	Au	Photolitho graphy	Yes	18
Cu^{2+}	3	10.7 (nA/ppb)	10-400 ppb	AuNPs modified Carbon	Printing techniques	No	39
Zn^{2+}, Cd^{2+}, Pb^{2+}, Cu^{2+}, and Hg^{2+}	-	4.1 (nA/ppb)	0 - 300 ppb	Au and Bi with Nafion	Photolitho graphy	No	58

Analyte	LOD	Sensitivity	Linear range	Electrode	Fabrication	Microfluidic	Ref
Cu^{2+}, Zn^{2+}	0.1	-	300–1500 ppb	Au modified $Ti_3C_2T_x$ and MWNTs	Photolithography	No	59
Zn^{2+}	-	-	0-2000 ppb	Au on glove	Shadow mask sputtering	No	60
Zn^{2+}	50	23.8 (nA/ppb)	100 -2000 ppb	Bismuth on Nafion and Carbon	Electroplating on printed Carbon electrode	No	61
Conductivity	-	13.9 (pF / (S ·m^{-1}))	0.000179 - 1.04 S·m^{-1}	Cu	Photolithography	Yes	62
Conductivity	-	2.4 (S/mM equiv. NaCl)	10-150 mM (equiv. NaCl)	Au	Photolithography	Yes	63
Cu^{2+}	396	2.3 (nA/ppb)	500-2500 ppb	Carbon paste	Screen printing	Yes	This study
Conductivity	-	$2.95 \cdot 10^{-6}$ S/mM (equi. NaCl)	5-165 mM	AgNPs	Inkjet printing	Yes	This study

Generally, the electrodes in the reported studies are composed of noble metal (*e.g.*, Au) fabricated with cleanroom facilities. The corresponding sensing systems lacks a microfluidic system to monitor the sweat rate and volume and work on the basis of commercial bulky potentiostat. In this study, simple printing techniques were harnessed to fabricate a microfluidic device to detect Cu^{2+} with measuring the conductivity and volume of sweat. The printed microfluidic system was used in conjunction with a customized wearable PCB board including a miniaturized potentiostat, the function of RI and wireless communication module with low-power consumption.

Despite the higher LOD of 396 ppb and lower sensitivity of 2.3 nA/ppb with respect to the majority of the technologies in literature (Table 4.1), which can be attributed to the heterogeneity nature of carbon paste surface, the clinically relevant concentrations of Cu in sweat was achieved. [50]

4.4 Conclusion

In this study, an all-printed microfluidic device for the detection of Cu^{2+} ions in artificial sweat in a wearable format was reported. With the purpose of normalizing Cu^{2+} concentration with sweat rate, two inkjet-printed nanosensors in the two-finger configuration were integrated in the microfluidic device to detect sweat conductivity and volume. Besides, a flexible PCB board was employed as a miniaturized potentiostat to operate SWASV in the microfluidic device, together with the function of RI aiming for active sampling. The LOD of the microfluidic device to detect Cu^{2+} ions was 396 ppb with sensitivity of 2.3 nA/ppb. Although the performance was not as good as the majority of the technologies reported in the literature, the microfluidic device offered a clinically relevant sensing range of Cu^{2+} in artificial sweat (240-2400 ppb). Moreover, compared to the sensors fabricated by traditional techniques, our all-printed wearable sensor brought its fabrication out of the cleanroom at low cost.

Reference

(1) Tat, T.; Chen, K.; Nashalian, A.; Chen, J. Wearable Physical Sensors. In *Wearable Physical, Chemical and Biological Sensors*; Moráles-Narvaez, E., Dincer, C., Eds.; 2022; pp 183–217.

(2) Kim, J.; Campbell, A. S.; de Ávila, B. E.-F.; Wang, J. Wearable Biosensors for Healthcare Monitoring. *Nat. Biotechnol.* **2019**, *37* (4), 389–406. https://doi.org/10.1038/s41587-019-0045-y.

(3) Garg, S. K.; Voelmle, M. K.; Gottlieb, P. Feasibility of 10-Day Use of a Continuous Glucose-Monitoring System in Adults With Type 1 Diabetes. *Diabetes Care* **2009**, *32* (3), 436–438. https://doi.org/10.2337/dc08-1745.

(4) Rosati, G.; Gherardi, G.; Grigoletto, D.; Marcolin, G.; Cancellara, P.; Mammucari, C.; Scaramuzza, M.; De Toni, A.; Reggiani, C.; Rizzuto, R.; Paccagnella, A. Lactate Dehydrogenase and Glutamate Pyruvate Transaminase Biosensing Strategies for Lactate Detection on Screen-Printed Sensors. Catalysis Efficiency and Interference Analysis in Complex Matrices: From Cell Cultures to Sport Medicine. *Sens. Bio-Sensing Res.* **2018**, *21*, 54–64. https://doi.org/https://doi.org/10.1016/j.sbsr.2018.10.004.

(5) Bariya, M.; Nyein, H. Y. Y.; Javey, A. Wearable Sweat Sensors. *Nat. Electron.* **2018**, *1* (3), 160–171. https://doi.org/10.1038/s41928-018-0043-y.

(6) Ghaffari, R.; Rogers, J. A.; Ray, T. R. Recent Progress, Challenges, and Opportunities for Wearable Biochemical Sensors for Sweat Analysis. *Sensors Actuators B Chem.* **2021**, *332*, 129447. https://doi.org/https://doi.org/10.1016/j.snb.2021.129447.

(7) Mohan, A. M. V.; Rajendran, V.; Mishra, R. K.; Jayaraman, M. Recent Advances and Perspectives in Sweat Based Wearable Electrochemical Sensors. *TrAC Trends Anal. Chem.* **2020**, *131*, 116024. https://doi.org/https://doi.org/10.1016/j.trac.2020.116024.

(8) Qiao, L.; Benzigar, M. R.; Subramony, J. A.; Lovell, N. H.; Liu, G. Advances in Sweat Wearables: Sample Extraction, Real-Time Biosensing, and Flexible Platforms. *ACS Appl. Mater. Interfaces* **2020**, *12* (30), 34337–34361. https://doi.org/10.1021/acsami.0c07614.

(9) Xu, J.; Fang, Y.; Chen, J. Wearable Biosensors for Non-Invasive Sweat Diagnostics. *Biosensors* . 2021. https://doi.org/10.3390/bios11080245.

(10) Jo, S.; Sung, D.; Kim, S.; Koo, J. A Review of Wearable Biosensors for Sweat Analysis. *Biomed. Eng. Lett.* **2021**, *11* (2), 117–129. https://doi.org/10.1007/s13534-021-00191-y.

(11) Brothers, M. C.; DeBrosse, M.; Grigsby, C. C.; Naik, R. R.; Hussain, S. M.; Heikenfeld, J.; Kim, S. S. Achievements and Challenges for Real-Time Sensing of Analytes in Sweat within Wearable Platforms. *Acc. Chem. Res.* **2019**, *52* (2), 297–306. https://doi.org/10.1021/acs.accounts.8b00555.

(12) Liu, C.; Xu, T.; Wang, D.; Zhang, X. The Role of Sampling in Wearable Sweat Sensors. *Talanta* **2020**, *212*, 120801. https://doi.org/https://doi.org/10.1016/j.talanta.2020.120801.

(13) Baker, L. B. Sweating Rate and Sweat Sodium Concentration in Athletes: A Review of Methodology and Intra/Interindividual Variability. *Sport. Med.* **2017**, *47* (1), 111–128. https://doi.org/10.1007/s40279-017-0691-5.

(14) Harshman, S. W.; Strayer, K. E.; Davidson, C. N.; Pitsch, R. L.; Narayanan, L.; Scott, A. M.; Schaeublin, N. M.; Wiens, T. L.; Phelps, M. S.; O'Connor, M. L.; Mackowski, N. S.; Barrett, K. N.; Leyh, S. M.; Eckerle, J. J.; Strang, A. J.; Martin, J. A. Rate Normalization for Sweat Metabolomics Biomarker

Discovery. *Talanta* **2021**, *223*, 121797. https://doi.org/https://doi.org/10.1016/j.talanta.2020.121797.

(15) Buono, M. J.; Ball, K. D.; Kolkhorst, F. W. Sodium Ion Concentration vs. Sweat Rate Relationship in Humans. *J. Appl. Physiol.* **2007**, *103* (3), 990–994. https://doi.org/10.1152/japplphysiol.00015.2007.

(16) Shamsuddin, A. K. M.; Yanagimoto, S.; Kuwahara, T.; Zhang, Y.; Nomura, C.; Kondo, N. Changes in the Index of Sweat Ion Concentration with Increasing Sweat during Passive Heat Stress in Humans. *Eur. J. Appl. Physiol.* **2005**, *94* (3), 292–297. https://doi.org/10.1007/s00421-005-1314-7.

(17) Salvo, P.; Di Francesco, F.; Costanzo, D.; Ferrari, C.; Trivella, M. G.; De Rossi, D. A Wearable Sensor for Measuring Sweat Rate. *IEEE Sens. J.* **2010**, *10* (10), 1557–1558. https://doi.org/10.1109/JSEN.2010.2046634.

(18) Nyein, H. Y. Y.; Tai, L.-C.; Ngo, Q. P.; Chao, M.; Zhang, G. B.; Gao, W.; Bariya, M.; Bullock, J.; Kim, H.; Fahad, H. M.; Javey, A. A Wearable Microfluidic Sensing Patch for Dynamic Sweat Secretion Analysis. *ACS Sensors* **2018**, *3* (5), 944–952. https://doi.org/10.1021/acssensors.7b00961.

(19) Vaquer, A.; Barón, E.; de la Rica, R. Wearable Analytical Platform with Enzyme-Modulated Dynamic Range for the Simultaneous Colorimetric Detection of Sweat Volume and Sweat Biomarkers. *ACS Sensors* **2021**, *6* (1), 130–136. https://doi.org/10.1021/acssensors.0c01980.

(20) Lee, H.-B.; Meeseepong, M.; Trung, T. Q.; Kim, B.-Y.; Lee, N.-E. A Wearable Lab-on-a-Patch Platform with Stretchable Nanostructured Biosensor for Non-Invasive Immunodetection of Biomarker in Sweat. *Biosens. Bioelectron.* **2020**, *156*, 112133. https://doi.org/https://doi.org/10.1016/j.bios.2020.112133.

(21) Zhang, Z.; Azizi, M.; Lee, M.; Davidowsky, P.; Lawrence, P.; Abbaspourrad, A. A Versatile, Cost-Effective, and Flexible Wearable Biosensor for in Situ and Ex Situ Sweat Analysis, and Personalized Nutrition Assessment. *Lab Chip* **2019**, *19* (20), 3448–3460. https://doi.org/10.1039/C9LC00734B.

(22) Vinoth, R.; Nakagawa, T.; Mathiyarasu, J.; Mohan, A. M. V. Fully Printed Wearable Microfluidic Devices for High-Throughput Sweat Sampling and Multiplexed Electrochemical Analysis. *ACS Sensors* **2021**, *6* (3), 1174–1186. https://doi.org/10.1021/acssensors.0c02446.

(23) Anastasova, S.; Crewther, B.; Bembnowicz, P.; Curto, V.; Ip, H. M. D.; Rosa, B.; Yang, G.-Z. A Wearable Multisensing Patch for Continuous Sweat Monitoring. *Biosens. Bioelectron.* **2017**, *93*, 139–145. https://doi.org/https://doi.org/10.1016/j.bios.2016.09.038.

(24) Lezana, J. L.; Vargas, M. H.; Karam-Bechara, J.; Aldana, R. S.; Furuya, M. E. Y. Sweat Conductivity and Chloride Titration for Cystic Fibrosis Diagnosis in 3834 Subjects. *J. Cyst. Fibros.* **2003**, *2* (1), 1–7. https://doi.org/https://doi.org/10.1016/S1569-1993(02)00146-7.

(25) Lilley, S. G.; Florence, T. M.; Stauber, J. L. The Use of Sweat to Monitor Lead Absorption through the Skin. *Sci. Total Environ.* **1988**, *76* (2), 267–278. https://doi.org/https://doi.org/10.1016/0048-9697(88)90112-X.

(26) Tang, S.; Yu, X.; Wu, C. Comparison of the Levels of Five Heavy Metals in Human Urine and Sweat after Strenuous Exercise by ICP-MS. *J. Appl. Math. Phys.* **2016**, *4*, 2.

(27) Jadoon, S.; Karim, S.; Akram, M. R.; Kalsoom Khan, A.; Zia, M. A.; Siddiqi, A. R.; Murtaza, G. Recent Developments in Sweat Analysis and Its Applications. *Int. J. Anal. Chem.* **2015**, *2015*, 164974. https://doi.org/10.1155/2015/164974.

(28) Criscuolo, F.; Ny Hanitra, I.; Aiassa, S.; Taurino, I.; Oliva, N.; Carrara, S.; De Micheli, G. Wearable Multifunctional Sweat-Sensing System for Efficient Healthcare Monitoring. *Sensors Actuators B Chem.* **2021**, *328*, 129017. https://doi.org/https://doi.org/10.1016/j.snb.2020.129017.

(29) Yu, L.; Liou, I. W.; Biggins, S. W.; Yeh, M.; Jalikis, F.; Chan, L.-N.; Burkhead, J. Copper Deficiency in Liver Diseases: A Case Series and Pathophysiological Considerations. *Hepatol. Commun.* **2019**, *3* (8), 1159–1165. https://doi.org/https://doi.org/10.1002/hep4.1393.

(30) Klevay, L. M. Coronary Heart Disease: The Zinc/Copper Hypothesis. *Am. J. Clin. Nutr.* **1975**, *28* (7), 764–774. https://doi.org/10.1093/ajcn/28.7.764.

(31) Youssef, A. A.; Wood, B.; Baron, D. N. Serum Copper: A Marker of Disease Activity in Rheumatoid Arthritis. *J. Clin. Pathol.* **1983**, *36* (1), 14–17. https://doi.org/10.1136/jcp.36.1.14.

(32) Schaefer, M.; Schellenberg, M.; Merle, U.; Weiss, K. H.; Stremmel, W. Wilson Protein Expression, Copper Excretion and Sweat Production in Sweat Glands of Wilson Disease Patients and Controls. *BMC Gastroenterol.* **2008**, *8* (1), 29. https://doi.org/10.1186/1471-230X-8-29.

(33) Agarwal, A.; Shilpa Avarebeel; Choudhary, N. S.; Goudar, M.; Tejaswini, C. . Correlation of Trace Elements in Patients of Chronic Liver Disease with Respect to Child- Turcotte- Pugh Scoring System. *Journal of Clinical and Diagnostic Research*. 2017, p OC25.

(34) Nangliya, V.; Sharma, A.; Yadav, D.; Sunder, S.; Nijhawan, S.; Mishra, S. Study of Trace Elements in Liver Cirrhosis Patients and Their Role in Prognosis of Disease. *Biol. Trace Elem. Res.* **2015**, *165* (1), 35–40. https://doi.org/10.1007/s12011-015-0237-3.

(35) Aruoma, O. I.; Reilly, T.; MacLaren, D.; Halliwell, B. Iron, Copper and Zinc Concentrations in Human Sweat and Plasma; the Effect of Exercise. *Clin. Chim. Acta* **1988**, *177* (1), 81–87. https://doi.org/https://doi.org/10.1016/0009-8981(88)90310-5.

(36) Gutteridge, J. M. C.; Rowley, D. A.; Halliwell, B.; Cooper, D. F.; Heeley, D. M. Copper and Iron Complexes Catalytic for Oxygen Radical Reactions in Sweat from Human Athletes. *Clin. Chim. Acta* **1985**, *145* (3), 267–273. https://doi.org/https://doi.org/10.1016/0009-8981(85)90033-6.

(37) Siquier-Coll, J.; Bartolomé, I.; Perez-Quintero, M.; Grijota, F. J.; Muñoz, D.; Maynar-Mariño, M. Effects of Exposure to High Temperatures on Serum, Urine and Sweat Concentrations of Iron and Copper. *J. Therm. Biol.* **2020**, *89*, 102536. https://doi.org/https://doi.org/10.1016/j.jtherbio.2020.102536.

(38) Souza, A. P. R. D.; Lima, A. S.; Salles, M. O.; Nascimento, A. N.; Bertotti, M. The Use of a Gold Disc Microelectrode for the Determination of Copper in Human Sweat. *Talanta* **2010**, *83* (1), 167–170. https://doi.org/10.1016/j.talanta.2010.09.001.

(39) Bagheri, N.; Mazzaracchio, V.; Cinti, S.; Colozza, N.; Di Natale, C.; Netti, P. A.; Saraji, M.; Roggero, S.; Moscone, D.; Arduini, F. Electroanalytical Sensor Based on Gold-Nanoparticle-Decorated Paper for Sensitive Detection of Copper Ions in Sweat and Serum. *Anal. Chem.* **2021**, *93* (12), 5225–5233. https://doi.org/10.1021/acs.analchem.0c05469.

(40) Silva, R. R.; Raymundo-Pereira, P. A.; Campos, A. M.; Wilson, D.; Otoni, C. G.; Barud, H. S.; Costa, C. A. R.; Domeneguetti, R. R.; Balogh, D. T.; Ribeiro, S. J. L.; Oliveira, O. N. Microbial Nanocellulose Adherent to Human Skin Used in Electrochemical Sensors to Detect Metal Ions and Biomarkers in Sweat. *Talanta* **2020**, *218* (January). https://doi.org/10.1016/j.talanta.2020.121153.

(41) Rosati, G.; Urban, M.; Zhao, L.; Yang, Q.; de Carvalho Castro e Silva, C.; Bonaldo, S.; Parolo, C.; Nguyen, E. P.; Ortega, G.; Fornasiero, P.; Paccagnella, A.; Merkoçi, A. A Plug, Print & Play Inkjet

Printing and Impedance-Based Biosensing Technology Operating through a Smartphone for Clinical Diagnostics. *Biosens. Bioelectron.* **2022**, *196*, 113737. https://doi.org/https://doi.org/10.1016/j.bios.2021.113737.

(42) Dong, H.; Li, C.-M.; Zhang, Y.-F.; Cao, X.-D.; Gan, Y. Screen-Printed Microfluidic Device for Electrochemical Immunoassay. *Lab Chip* **2007**, *7* (12), 1752–1758. https://doi.org/10.1039/B712394A.

(43) Haynes, W. M.; Lide, D. R.; Bruno, T. J. *CRC Handbook of Chemistry and Physics*, 97th Editi.; 2016. https://doi.org/https://doi.org/10.1201/9781315380476.

(44) Moonen, E. J. M.; Haakma, J. R.; Peri, E.; Pelssers, E.; Mischi, M.; den Toonder, J. M. J. Wearable Sweat Sensing for Prolonged, Semicontinuous, and Nonobtrusive Health Monitoring. *VIEW* **2020**, *1* (4), 20200077. https://doi.org/https://doi.org/10.1002/VIW.20200077.

(45) Trung, T. Q.; Lee, N.-E. Flexible and Stretchable Physical Sensor Integrated Platforms for Wearable Human-Activity Monitoringand Personal Healthcare. *Adv. Mater.* **2016**, *28* (22), 4338–4372. https://doi.org/https://doi.org/10.1002/adma.201504244.

(46) Sato, K.; Sato, F. Individual Variations in Structure and Function of Human Eccrine Sweat Gland. *Am. J. Physiol. Integr. Comp. Physiol.* **1983**, *245* (2), R203–R208. https://doi.org/10.1152/ajpregu.1983.245.2.R203.

(47) Buono, M. J.; Connolly, K. P. Increases in Sweat Rate during Exercise: Gland Recruitment versus Output per Gland. *J. Therm. Biol.* **1992**, *17* (4), 267–270. https://doi.org/https://doi.org/10.1016/0306-4565(92)90065-N.

(48) Taylor, N. A. S.; Machado-Moreira, C. A. Regional Variations in Transepidermal Water Loss, Eccrine Sweat Gland Density, Sweat Secretion Rates and Electrolyte Composition in Resting and Exercising Humans. *Extrem. Physiol. Med.* **2013**, *2* (1), 4. https://doi.org/10.1186/2046-7648-2-4.

(49) Jian, J.-M.; Liu, Y.-Y.; Zhang, Y.-L.; Guo, X.-S.; Cai, Q. Fast and Sensitive Detection of Pb2+ in Foods Using Disposable Screen-Printed Electrode Modified by Reduced Graphene Oxide. *Sensors* . 2013. https://doi.org/10.3390/s131013063.

(50) Hohnadel, D. C.; Sunderman Jr., F. W.; Nechay, M. W.; McNeely, M. D. Atomic Absorption Spectrometry of Nickel, Copper, Zinc, and Lead in Sweat Collected from Healthy Subjects during Sauna Bathing. *Clin. Chem.* **1973**, *19* (11), 1288–1292. https://doi.org/10.1093/clinchem/19.11.1288.

(51) Pérez-Ràfols, C.; Serrano, N.; Díaz-Cruz, J. M.; Ariño, C.; Esteban, M. Glutathione Modified Screen-Printed Carbon Nanofiber Electrode for the Voltammetric Determination of Metal Ions in Natural Samples. *Talanta* **2016**, *155*, 8–13. https://doi.org/https://doi.org/10.1016/j.talanta.2016.04.011.

(52) Ghanei-Motlagh, M.; Karami, C.; Taher, M. A.; Hosseini-Nasab, S. J. Stripping Voltammetric Detection of Copper Ions Using Carbon Paste Electrode Modified with Aza-Crown Ether Capped Gold Nanoparticles and Reduced Graphene Oxide. *RSC Adv.* **2016**, *6* (92), 89167–89175. https://doi.org/10.1039/C6RA10267K.

(53) Hutton, L. A.; Newton, M. E.; Unwin, P. R.; Macpherson, J. V. Factors Controlling Stripping Voltammetry of Lead at Polycrystalline Boron Doped Diamond Electrodes: New Insights from High-Resolution Microscopy. *Anal. Chem.* **2011**, *83* (3), 735–745. https://doi.org/10.1021/ac101626s.

(54) Kuo, S.-H.; Shen, C.-J.; Shen, C.-F.; Cheng, C.-M. Role of PH Value in Clinically Relevant Diagnosis. *Diagnostics (Basel, Switzerland)* **2020**, *10* (2). https://doi.org/10.3390/diagnostics10020107.

(55)   Rao, G.; Guy, R. H.; Glikfeld, P.; LaCourse, W. R.; Leung, L.; Tamada, J.; Potts, R. O.; Azimi, N. Reverse Iontophoresis: Noninvasive Glucose Monitoring in Vivo in Humans. *Pharm. Res.* **1995**, *12* (12), 1869–1873. https://doi.org/10.1023/A:1016271301814.

(56)   Leboulanger, B.; Guy, R. H.; Delgado-Charro, M. B. Reverse Iontophoresis for Non-Invasive Transdermal Monitoring. *Physiol. Meas.* **2004**, *25* (3), R35--R50. https://doi.org/10.1088/0967-3334/25/3/r01.

(57)   Giri, T. K.; Chakrabarty, S.; Ghosh, B. Transdermal Reverse Iontophoresis: A Novel Technique for Therapeutic Drug Monitoring. *J. Control. Release* **2017**, *246*, 30–38. https://doi.org/https://doi.org/10.1016/j.jconrel.2016.12.007.

(58)   Gao, W.; Nyein, H. Y. Y.; Shahpar, Z.; Fahad, H. M.; Chen, K.; Emaminejad, S.; Gao, Y.; Tai, L. C.; Ota, H.; Wu, E.; Bullock, J.; Zeng, Y.; Lien, D. H.; Javey, A. Wearable Microsensor Array for Multiplexed Heavy Metal Monitoring of Body Fluids. *ACS Sensors* **2016**, *1* (7), 866–874. https://doi.org/10.1021/acssensors.6b00287.

(59)   Park, J. Y.; Hui, X.; Sharifuzzaman, M.; Sharma, S.; Xuan, X.; Zhang, S.; Ko, S. G.; Yoon, S. H. High-Performance Flexible Electrochemical Heavy Metal Sensor Based on Layer-by-Layer Assembly of Ti3C2Tx/MWNTs Nanocomposites for Noninvasive Detection of Copper and Zinc Ions in Human Biofluids. *ACS Appl. Mater. Interfaces* **2020**, *12* (43), 48928–48937. https://doi.org/10.1021/acsami.0c12239.

(60)   Mallika, B.; Lu, L.; Rahul, G.; Heera, A. C.; Yin, N. H. Y.; Li-Chia, T.; Ali, J. Glove-Based Sensors for Multimodal Monitoring of Natural Sweat. *Sci. Adv.* **2021**, *6* (35), eabb8308. https://doi.org/10.1126/sciadv.abb8308.

(61)   Kim, J.; De Araujo, W. R.; Samek, I. A.; Bandodkar, A. J.; Jia, W.; Brunetti, B.; Paixão, T. R. L. C.; Wang, J. Wearable Temporary Tattoo Sensor for Real-Time Trace Metal Monitoring in Human Sweat. *Electrochem. commun.* **2015**, *51*, 41–45. https://doi.org/10.1016/j.elecom.2014.11.024.

(62)   Hourlier-Fargette, A.; Schon, S.; Xue, Y.; Avila, R.; Li, W.; Gao, Y.; Liu, C.; Kim, S. B.; Raj, M. S.; Fields, K. B.; Parsons, B. V; Lee, K.; Lee, J. Y.; Chung, H. U.; Lee, S. P.; Johnson, M.; Bandodkar, A. J.; Gutruf, P.; Model, J. B.; Aranyosi, A. J.; Choi, J.; Ray, T. R.; Ghaffari, R.; Huang, Y.; Rogers, J. A. Skin-Interfaced Soft Microfluidic Systems with Modular and Reusable Electronics for in Situ Capacitive Sensing of Sweat Loss, Rate and Conductivity. *Lab Chip* **2020**, *20* (23), 4391–4403. https://doi.org/10.1039/D0LC00705F.

(63)   Steijlen, A. S. M.; Bastemeijer, J.; Jansen, K. M. B.; French, P. J.; Bossche, A. A Novel Sweat Rate and Conductivity Sensor Patch Made with Low-Cost Fabrication Techniques. In *2020 IEEE SENSORS*; 2020; pp 1–4. https://doi.org/10.1109/SENSORS47125.2020.9278850.

Chapter 5

Chapter 5: Conclusion

The detailed conclusion of each chapter is mentioned at the end of the corresponding presented work. In this part, according to the motivation and objectives in Chapter 1.4 and the results in Chapter 2-4, the general conclusion, shortcomings, and future perspectives are discussed in this chapter.

To fill the blank space of *in-situ* HMIs detection, which is difficult to be covered by conventional methods, we demonstrate the electrochemical sensing systems by SWASV technique to be used in environmental monitoring and healthcare in this thesis, featuring simplicity, low cost, and integration.

i. Firstly, a robust electrochemical HMIs sensing system was developed on the basis of the fluidic system, which allowed for automatic sampling, mixing, and testing required by *in-situ* measurement. The LODs of Cd^{2+}, Pb^{2+}, and Cu^{2+} were at ppb level. More interestingly, this fluidic sensing system was integrated into an autonomous boat to challenge the shortage of the presented electrochemical platforms for the spatial risk assessment of HMs in natural waters. The autonomous sensing boat was tested during a campaign, and navigated under the programmable path automatically. This sensing boat also distinguished the highest concentration of Pb^{2+} in the effluent sample compared to other normal sites in the stream. Despite this, the HM sensing boat cannot respond to uncertainties perfectly in our study, for the *in-situ* measurement was disrupted by the unexpected hydro morphology. Instead, in-field measurements were operated in our case. To address this problem, the camera module would be integrated into the boat, which may be trained to respond to various situations *via* computing vision in the future.

ii. In addition, the SPCE applied in this electrochemical sensing system demonstrated a poor sensing signal of Cd^{2+} ions co-existing with Cu^{2+} and Pb^{2+} in the tested solution, which is ascribed to the mutual interference problem. In Chapter 1.3, nanomaterials seem appealing due to their large surface area and tunable surface chemistry. Hence, in this work, an innovative graphene derivative with the covalently bound thiol moieties on its surface (GSH) was utilized to modify SPCE for mitigating the mutual interference effect. After modification, SPCE demonstrated statically significant enhancement of Cd^{2+} sensitivity compared to the bare SPCE; however, the sensitivity of Pb^{2+} and Cu^{2+} were not influenced. This phenomenon could be ascribed to the better affinity offered by thiol moieties to Cd^{2+} rather than Pb^{2+} and Cu^{2+} based on HASB theory. Lastly, GSH-SPCE obtained the LODs of Cd^{2+}, Pb^{2+}, and Cu^{2+} at 15 ppb, 10ppb, and 6 ppb, respectively.

iii.   To simplify this electrochemical sensing system and apply it as a wearable sensor to monitor the HMIs in sweat, this focuses on the design and fabrication of a microfluidic sensing device that drove the artificial sweat by capillarity to replace the pump with light weightiness. Unlike most reported wearable devices that were fabricated in a cleaning room by photolithography, various printing techniques such as screen printing, inkjet printing, and wax printing were used to fabricate an all-printed sensing device in a mass produced way. Besides, the printed conductivity and volume nanosensors were integrated into the system too, with the interest of compensating the inaccuracy when the sweat rate is too fast or slow. Additionally, to be more compact, a flexible customized mini-potentiostat was applied to replace the commercial bulky potentiostat and was validated with the microfluidic sensing device. Even though many issues remained, such as the real validation of sampling and testing on human subjects, the limitation of deposition potential by the hardware, and accidental bubble issues, this work still demonstrate great potential of combining diverse printing technologies to lower the cost in wearable HM sensing devices for healthcare.